Remote Sensing of Environment 303 (2024) 113998

Contents lists available at ScienceDirect

Remote Sensing of Environment

journal homepage: www.elsevier.com/locate/rse

Estimation of global transpiration from remotely sensed solar-induced chlorophyll fluorescence

Jingjing Yang [a,b,c], Zhunqiao Liu [d], Qiang Yu [d], Xiaoliang Lu [d,*]

[a] The Research Center of Soil and Water Conservation and Ecological Environment, Chinese Academy of Sciences and Ministry of Education, Yangling, Shaanxi 712100, China
[b] Institute of Soil and Water Conservation, Chinese Academy of Sciences and Ministry of Water Resources, Yangling, Shaanxi 712100, China
[c] University of Chinese Academy of Sciences, Beijing 100049, China
[d] State Key Laboratory of Soil Erosion and Dryland Farming on the Loess Plateau, Northwest A&F University, Yangling, Shaanxi 712100, China

ARTICLE INFO

Edited by Jing M. Chen

Keywords:
Solar-induced fluorescence
Ecosystem transpiration
Canopy conductance
the Penman-Monteith (PM) equation
and the mechanistic model

ABSTRACT

Accurate estimation of ecosystem transpiration (T) is critical to understanding of global land-atmosphere water, energy and carbon fluxes. However, the complexity of processes governing canopy conductance to transpired water vapor (G_c) poses a substantial challenge for modelling T. Canopy conductance governs the uptake of CO_2 for photosynthesis and the release of water vapor through transpiration, and so satellite observations of solar-induced chlorophyll fluorescence (SIF), a new proxy for plant photosynthesis, may create a good opportunity to estimate T at large scales. In this study, a new SIF-based model is proposed to estimate T at the canopy scale: photosynthesis rate, a key input for the coupled photosynthesis–stomatal conductance framework, is mechanistically approximated from top-of-canopy (TOC) SIF and readily-available meteorological data. One major improvement makes our work conceptually novel, compared to previous T modelling efforts: SIF is mechanistically translated into photosynthetic CO_2 assimilation such that the regulation of G_c and eventually T can be realized in a more physiologically realistic way. We evaluate the modeled T forced by satellite SIF observations and globally gridded meteorological information at 31 eddy covariance flux sites covering ten vegetation types in three continents. The model performs well in various vegetation types, particularly in ecosystems with dense canopies, explaining nearly 76% of the variability in their daily flux-derived T. We apply the model to obtain the spatial and temporal distributions of global T at a daily time step for the period 2019–2020, and diagnose the response of T to vapor pressure deficit (VPD) and soil water content (SWC). At the global scale, increasing VPD exhibits a negative correlation with G_c but a positive correlation with T, and their correlations decrease with decreasing SWC. In contrast, a decrease in SWC is not associated with a clear reduction in G_c and T as long as the SWC is not low. Our proposed model better unleashes the potential of SIF in modelling T, and thus opens a new pathway to better understand the mechanisms impacting the coupling of carbon and water cycles.

1. Introduction

Ecosystem transpiration (T) which represents water loss as vapor from the leaf surface to the atmosphere, primarily through leaf stomata, accounts for approximately 65% of global land surface evapotranspiration (ET, Good et al., 2015). In vegetated ecosystems with a dense canopy, transpiration may contribute up to 90% of evapotranspiration (Jasechko et al., 2013). Thus, transpiration plays a critical role in the global water and carbon cycles and in the land-surface energy budget (Fisher et al., 2017; Trenberth et al., 2009). Remote sensing-based ET models are dominant for making ET/T estimations at regional and global scales (Long and Singh, 2012; Mu et al., 2007; Mu et al., 2011; Ryu et al., 2011; Yang and Shang, 2013; Zhang et al., 2017), and, among them, the approaches that combine the Penman-Monteith (PM) logic (Monteith, 1965) with meteorological forcing and remotely sensed vegetation parameters have a robust theoretical basis while being relatively simple (Cleugh et al., 2007; Leuning et al., 2008; Mu et al., 2007; Mu et al., 2011). For example, the PM-based modelling framework from the MODerate resolution Imaging Spectroradiometer (MODIS) ET product (MOD16, Mu et al., 2007; Mu et al., 2011) is now widely used for mapping global ET/T. The Priestley-Taylor (PT) equation (Priestley and Taylor, 1972) offers a simplified version of the PM equation. By reducing

* Corresponding author.
E-mail address: luxiaoliang@nwafu.edu.cn (X. Lu).

https://doi.org/10.1016/j.rse.2024.113998
Received 2 August 2023; Received in revised form 1 January 2024; Accepted 11 January 2024
Available online 18 January 2024

the requirement on inputs and parameters, it has still demonstrated its effectiveness as an alternative, particularly in situations where net radiation to the canopy is the primary determinant of ET (Norman et al., 1995). Based on the PT equation, for example, the Global Land Evaporation Amsterdam Model (GLEAM) combines a wide range of remotely sensed observations to derive global daily actual ET and its different components with a spatial resolution of 0.25 degrees (Martens et al., 2017; Miralles et al., 2016).As transpiration loss is closely linked to carbon assimilation via stomatal conductance, photosynthetic CO_2 assimilation is expected to have a strong correlation with T. During photosynthesis, most of the absorbed photosynthetically active radiation (APAR) is consumed in carbon fixation and heat loss (non-photochemical quenching, NPQ). About 1–2% of APAR is reemitted by chlorophyll (Chl) molecules in the spectral range 640–850 nm and is referred to as solar-induced chlorophyll fluorescence (SIF). There are two photosystems in the chloroplasts of plants: Photosystem I (PSI) and Photosystem II (PSII). SIF is emitted from both photosystems: SIF from PSI is mostly in the near-infrared (NIR) range (>700 nm), while SIF from PSII covers the full SIF spectrum. Numerous studies have shown that SIF observations have a strong ability to predict ecosystem gross primary production (GPP) over several terrestrial ecosystems including temperate deciduous forest (Yang et al., 2017; Yang et al., 2015), crops (He et al., 2020; Hwang et al., 2020), and evergreen needleleaf forest (Kim et al., 2021; Magney et al., 2019). Over the last decade, advances in the spectral and radiometric sensitivities of space-borne instruments have enabled us to retrieve SIF signals from space (Frankenberg et al., 2011; Guanter et al., 2012; Joiner et al., 2013). In particular, the TROPOspheric Monitoring Instrument (TROPOMI) onboard the Sentinel-5 Precursor provides SIF products with a spatial resolution of up to 7 × 3.5 km^2 (at nadir), and has a 16-day revisit cycle. Due to its wide swath width of 2600 km across track, TROPOMI can achieve near-daily global coverage (Köhler et al., 2018). All this progress has created a good opportunity to map large-scale T from SIF observations. Several SIF-based approaches have been proposed to estimate T, and generally they can be grouped into two types: (1) the empirical approaches (Lu et al., 2018; Maes et al., 2020) that link SIF with T using statistical models, by assuming that SIF is a proxy for all related factors regulating T, and (2) the process-based approaches (Shan et al., 2019, 2021) such as using the PM equation to calculate latent heat (λE, the energy consumption of ET) by establishing empirical/semi-mechanistic relationships between SIF and canopy conductance to transpired water vapor (G_c), one key input for the PM equation. Compared with the conventional modelling of T as a function of meteorological and vegetation indices, SIF-informed T approaches have the potential to better account for the impacts of plant physiological status on the transpiration flux.

Despite some success in predicting T from SIF, these methods may have the following limitations: (1) SIF is still empirically related to either G_c or T, resulting in an insufficient understanding of the mechanisms regulating T dynamics, (2) the SIF-G_c/T relationships must be trained at eddy covariance (EC) flux sites, and thus their performance may decrease in heterogeneous regions (Desai, 2010), and (3) the data-driven upscaling methods that provide regional estimates of T may also have significant uncertainties (Xiao et al., 2014; Xiao et al., 2011). To overcome these limitations, a more process-based understanding of the relationship between stomatal conductance and SIF needs to be established to correctly use SIF as a proxy for transpiration.

The mechanistic light response (MLR) model proposed by Gu et al. (2019) provides a robust basis for estimating GPP (and potentially T) from SIF observations (i.e., EC observations are essentially not required). However, the difficulty in obtaining the fraction of open PSII reaction centers (q_L, Kramer et al., 2004), a key input for the MLR model, restricts its practical application (Gu et al., 2019). Liu et al. (2022) reformulated the original MLR model (hereafter referred to as the rMLR model, Eq. (4)) by replacing q_L with two variables (the quantum yield of photochemical quenching in PSII (Φ_{PSII}), and NPQ) readily obtained at the canopy scale, thus facilitating the operational estimation of GPP on regional or global scales.

Here, we developed a mechanistic model, based on the rMLR model, to estimate ecosystem T from top-of-canopy (TOC) SIF signals. Using satellite SIF measurements as an input, the rMLR model was first employed to approximate net CO_2 uptake in the stomatal conductance estimation equation originally proposed by Ball, Woodrow and Berry (Ball et al., 1987) and modified by Wang and Leuning (1998), denoted here as the BWB-Leuning equation, to better constrain G_c. The PM equation, fed with meteorological forcings and SIF-informed G_c, was then used to obtain T. Compared to prior T estimation models, the proposed mechanistic model eliminates the reliance on EC measurements, thereby facilitating the estimation of transpiration in areas with sparse instrumentation. Further, the physiological information contained in SIF observations can be more realistically represented, providing a strong basis for modelling of canopy conductance. This framework was applied to produce the daily global T for the period 2019–2020. We evaluated the proposed model against EC observations at site scale, and against the T estimates based on MODIS and GLEAM (v3.8a) at the global scale.

2. Model description

2.1. Estimation of ecosystem T

The PM equation was used to estimate ecosystem T (g m^{-2} s^{-1}):

$$T = \frac{\Delta \times (R_n - G) + \rho \times C_p \times \mathrm{VPD} \times g_a}{\Delta + (1 + g_a/G_c) \times \gamma} \times \frac{1}{\lambda_v} \quad (1)$$

where Δ is the slope of saturated water-vapor pressure with air temperature (T_{air}, °C), assumed to be 0.155 kPa $°C^{-1}$; R_n is the net radiation (W m^{-2}); G is the soil heat flux (W m^{-2}); ρ is the density of dry air (≈ 1.2 kg m^{-3}); C_p is the specific heat capacity of air (≈ 1013 J kg^{-1} $°C^{-1}$); VPD is the atmospheric vapor pressure deficit (kPa); g_a is the aerodynamic resistance for heat and water vapor (m s^{-1}), and is estimated from air temperature (Text S1) (Thornton, 1998); γ is the psychometric constant (≈ 0.067 kPa $°C^{-1}$); λ_v is the latent heat of vaporization (≈ 2450 kJ kg^{-1}); G_c (m s^{-1}) is assumed to be equal to the surface conductance for dense canopies during the growing season.

2.2. Estimation of G_c

The main focus of the PM equation is the accurate estimate of G_c. In this study, the modified BWB-Leuning equation (Wang and Leuning, 1998) was used to calculate G_c:

$$G_c = G_o + \frac{a \times f_w \times A_{net}}{C_s \times (1 + \mathrm{VPD}/D_0)} \quad (2)$$

where G_o is the residual conductance (≈ 0.01 mol m^{-2} s^{-1}); a and D_0 are both empirical parameters, assumed to be 10 and 1.5 (Arain et al., 2002; Wang and Leuning, 1998; Miner et al., 2017), respectively; f_w is a factor representing the sensitivity of leaf stomatal conductance to soil water supply (Wang et al., 2018); A_{net} is the net photosynthetic rate (μmol m^{-2} s^{-1}) provided by the rMLR model using TOC SIF as an input (see below); C_s is the CO_2 concentration at the leaf surface (μmol mol^{-1}), assumed to be the product of $a/(a\text{-}1)$ and the intercellular CO_2 concentration (C_i, μmol mol^{-1}).

As the MODIS T estimates (T_{MODIS}) were also produced in this study for comparison purposes, here we briefly introduce the MOD16 algorithm (version 6.0) for estimating G_c (G_{c_MODIS}, hereafter). In MOD16, G_{c_MODIS} is modeled as (Running and Kimball, 2005; Thornton, 1998):

$$G_{\text{bad hbox}} = \begin{cases} \dfrac{G_s^2 \times (G_s^1 + G_{CU})}{G_s^1 + G_s^2 + G_{CU}} \times \text{LAI} \times (1 - F_{wet})(\text{LAI} > 0, (1 - F_{wet}) > 0) \\ 0(\text{LAI} = 0, (1 - F_{wet}) = 0) \end{cases} \tag{3a}$$

$$F_{wet} = \begin{cases} 0 RH < 70\% \\ RH^4 70\% \leqslant RH \leqslant 100\% \end{cases} \tag{3b}$$

where G_s^2 is leaf boundary-layer conductance, and equivalent to the leaf conductance to sensible heat per unit leaf area; G_s^1 is stomatal conductance per unit leaf area; G_{CU} is leaf cuticular conductance per unit leaf area; LAI is leaf area index; F_{wet} is water cover fraction (%); and RH is relative humidity (%) estimated from VPD; G_s^2 is a constant value for each given vegetation type; G_s^1 is a function of T_{air} and VPD; G_{CU} is estimated from T_{air}. Both G_s^1 and G_{CU} are also dependent on a variety of biome-specific parameters. Note that MOD16 assumes that all leaves in the canopy have the same leaf stomatal conductance, and upscales to the canopy level, namely $G_{\text{c\_MODIS}}$, by a factor of LAI.

The GLEAM model does not explicitly parameterize G_c. Instead, it first calculates the potential ET based on the PT equation and then adjusts this potential ET to actual ET by applying a series of stress factors. Ecosystem T is then determined by subtracting the evaporation of intercepted rainfall from actual ET. The more details for GLEAM in estimating T can be found in Text S2.

2.3. The rMLR model

The rMLR model (Liu et al., 2022) showed that GPP for C3 and C4 species at canopy or ecosystem scale can be mechanistically estimated as:

$$A_{\text{net}} = \begin{cases} \dfrac{C_c - \Gamma^*}{4C_c + 8\Gamma^*} \times \dfrac{\Phi_{\text{PSII}} \times (1 + \text{NPQ}) \times (1 + K_{\text{DF}}) \times \text{SIF}_{\text{TOC\_PSII\_FULL}}}{(1 - \Phi_{\text{PSII}}) \times f_{\text{esc\_P-C}}} - R_d & \text{C3} \\ \dfrac{(1 - \xi)}{3} \times \dfrac{\Phi_{\text{PSII}} \times (1 + \text{NPQ}) \times (1 + K_{\text{DF}}) \times \text{SIF}_{\text{TOC\_PSII\_FULL}}}{(1 - \Phi_{\text{PSII}}) \times f_{\text{esc\_P-C}}} - R_d & \text{C4} \end{cases} \tag{4}$$

where C_c is the chloroplastic CO_2 partial pressure (μbar or μmol mol^{-1}); Γ^* is the chloroplastic compensation point of CO_2 (μbar); Φ_{PSII} is the quantum yield of photochemical quenching in PSII; NPQ is non-photochemical quenching; K_{DF} is the ratio between the rate constants for constitutive heat loss and fluorescence, assumed to be 9.0 (Liu et al., 2022); $\text{SIF}_{\text{TOC\_FULL\_PSII}}$ is TOC broadband SIF (640–850 nm) emitted from PSII (μmol m^{-2} s^{-1}); $f_{\text{esc\_P-C}}$ is the probability that a SIF photon escapes from the PSII light reactions inside the leaves to the top of the canopy; R_d is the daytime leaf dark respiration (μmol m^{-2} s^{-1}); ξ is the fraction of total electron transport of mesophyll and bundle sheath allocated to mesophyll, assumed to be 0.4 (Von Caemmerer, 2000). Here, the mesophyll conductance to CO_2 was assumed to be infinite (van der Tol et al., 2009), and thus $C_c = C_i$.

According to Bacour et al. (2019), Φ_{PSII} is calculated as:

$$\Phi_{\text{PSII}} = \frac{min(\text{ETR}, \text{ETR}_{\text{c\_PSII}})}{\text{PAR} \times f_{\text{PAR}} \times \beta} \tag{5}$$

Where ETR (μmol m^{-2} s^{-1}) and $\text{ETR}_{\text{c\_PSII}}$ (μmol m^{-2} s^{-1}) are the electron transport rates in photosynthesis under light-limited and Rubisco-limited conditions, respectively; PAR is incoming photosynthetically active radiation (μmol m^{-2} s^{-1}), and was calculated from the incoming shortwave radiation (SW, W m^{-2}) data by multiplying 0.5 (Sancho-Knapik et al., 2022); f_{PAR} is the fraction of absorbed PAR; β is the partitioning of energy between the two photosystems, which is assumed to be equal (i.e., $\beta = 0.5$). ETR is estimated as:

$$\text{ETR} = \frac{\left(\text{PAR} \times f_{\text{PAR}} \times \beta + J_{\max} - \sqrt{(\text{PAR} \times f_{\text{PAR}} \times \beta + J_{\max})^2 - 4\theta \times J_{\max} \times \text{PAR} \times f_{\text{PAR}} \times \beta}\right)}{2\theta} \tag{6}$$

where θ is the convexity of the response curve of ETR to light absorbed by photosynthetic pigments (= 0.7, Von Caemmerer, 2000); $J_{\max}$ is the maximum value of ETR under saturated light (μmol m^{-2} s^{-1}), and can be expressed as (June et al., 2004):

$$J_{\max} = J_{max\_25} \times exp^{-\left(\frac{T_{\text{air}} - 25}{18}\right)^2} \tag{7a}$$

$$J_{max\_25} = (2.59 - 0.035 \times T\text{air}) \times V_{\text{cmax25}} \tag{7b}$$

where $J_{\text{max\_25}}$ is $J_{\max}$ at a reference temperature of (usually) 25 °C; V_{cmax25} is the maximum carboxylation rate at 25 °C (μmol m^{-2} s^{-1}), and can be estimated from leaf chlorophyll content (see section 3.1.1).

$\text{ETR}_{\text{c\_PSII}}$ is calculated as:

$$\text{ETR}_{\text{c\_PSII}} = \frac{A_c + R_d}{(C_i - \Gamma^*)/(4C_i + 8\Gamma^*)} \tag{8a}$$

$$A_c = \frac{(C_i - \Gamma^*) \times V_{\text{cmax}}}{C_i + K_c(1 + O/K_o)} - R_d \tag{8b}$$

where A_c is the Rubiso-limited gross photosynthesis rate (μmol m^{-2} s^{-1}); V_{cmax} is the maximum carboxylation rate (μmol m^{-2} s^{-1}); O is the intercellular oxygen concentration (Wu et al., 2017; Yin and Struik, 2009), assumed to be 210,000 mol mol^{-1}; K_c and K_o are the Michaelis-Menten constants for CO_2 (mol mol^{-1}) and O_2 (mol mol^{-1}), respectively.

K_c is calculated as (Yin and Struik, 2009):

$$K_c = K_{c25} \times exp(T_{\text{air}} - 25) \times E_{Kc} / \left(298 \times R_{\text{gas}} \times (T_{\text{air}} + 273)\right) \tag{9}$$

where K_{c25} is the Michaelis-Menten constant for CO_2 at 25 °C (= 270 mol mol^{-1}); E_{Kc} is approximately equal to 80,990 J mol^{-1} (Bernacchi et al., 2002) and R_{gas} is the molar gas constant (8.3143 m^3 Pa mol^{-1} K^{-1}).

K_o is calculated as (Yin and Struik, 2009):

$$K_o = K_{o25} \times exp(T_{\text{air}} - 25) \times E_{Ko} / \left(298 \times R_{\text{gas}} \times (T_{\text{air}} + 273)\right) \tag{10}$$

where K_{o25} is the Michaelis-Menten constant for O_2 at 25 °C (= 165,000 mol mol^{-1}); E_{Ko} is approximately equal to 23,720 J mol^{-1} (Bernacchi et al., 2002).

V_{cmax} can be calculated as (Yin and Struik, 2009):

$$V_{\text{cmax}} = V_{\text{cmax25}} \times exp(T_{\text{air}} - 25) \times E_{V\text{cmax}} / \left(298 \times R_{\text{gas}} \times (T_{\text{air}} + 273)\right) \tag{11}$$

where $E_{V\text{cmax}}$ is approximately equal to 65,330 (J mol^{-1}) (Bernacchi et al., 2002).

R_d can be expressed as (Yin and Struik, 2009):

$$R_d = R_{d25} \times exp(T_{\text{air}} - 25) \times E_{R_d} / \left(298 \times R_{\text{gas}} \times (T_{\text{air}} + 273)\right) \tag{12}$$

where R_{d25} is daytime leaf dark respiration at 25 °C (μmol m^{-2} s^{-1}), and can be computed as: $R_{d25} = 0.015 \times V_{\text{cmax25}}$ (Atkin et al., 2015); E_{Rd} is the temperature response of the R_d used to predict CO_2 uptake by leaves

during Rubisco-limited photosynthesis (≈ 46,390 J mol^{-1}, Bernacchi et al., 2001; Yin and Struik, 2009).

Γ^* was estimated as (Yin and Struik, 2009):

$$\Gamma^* = \frac{0.5 \times O}{S_{C/O}} \tag{13}$$

where the factor 0.5 is mol CO_2 released when Rubisco catalyses the reaction with 1 mol O_2 in photorespiration (Farquhar et al., 1980); $S_{C/O}$ (bar bar^{-1}) can be used to explain the decline of the Rubisco affinity for CO_2 with increasing temperature, and can be calculated as:

$$S_{C/O} = S_{C/O25} \times exp(T\text{air} - 25) \times ES_{C/O} / (298 \times R\text{gas} \times (T\text{air} + 273)) \tag{14}$$

where $S_{C/O25}$ and $E_{Sc/o}$ are approximately equal to 2800 (bar bar^{-1}) and − 24,460 (J mol^{-1}), respectively (Bernacchi et al., 2002).

NPQ is modeled as a function of T_{air} and PAR (Bacour et al., 2019):

$$\mathrm{NPQ} = \mathrm{a} \times \chi^{\mathrm{c}} \times \frac{1 + \mathrm{b}}{\mathrm{b} + \chi^{\mathrm{c}}} \times \frac{exp^{(\mathrm{d} \times T_{\mathrm{air}} + \mathrm{e})}}{\mathrm{PAR}^{f}} \tag{15}$$

The fitting parameters: a (16.042), b (5.74), c (2.167), d (−0.014), e (−0.00437), and f (0.000576), are provided by (Bacour et al., 2019); χ is defined as follows (van der Tol et al., 2014):

$$\chi = 1 - \frac{\Phi_{\mathrm{PSII}}}{\Phi_{\mathrm{PSII\_}max}} \tag{16}$$

where Φ_{PSII_max} is the maximum photosynthetic yield at the fully dark-adapted photosystems, typically taken as 0.80. Altogether, T_{air}, PAR, and f_{PAR} are needed to estimate Φ_{PSII} and NPQ.

2.4. Estimation of $SIF_{TOC\_FULL\_PSII}$ and $f_{esc\_P\text{-}C}$

$SIF_{TOC\_FULL\_PSII}$ should be obtained from remotely sensed TOC SIF observations: they are narrowband and contain contributions from both PSI and PSII. First, the ChlF contribution from PSII (f_{PSII}, %) to TOC SIF at a given wavelength λ nm ($SIF_{TOC}(\lambda)$, mW m^{-2} nm^{-1} sr^{-1}) has to be determined. Bacour et al. (2019) **showed that f_{PSII} can be estimated as:**

$$f_{\mathrm{PSII}} = \frac{m_2 \times \Phi_{\mathrm{F\_PSII}} / \Phi_{\mathrm{F0\_PSII}}}{m_1 + m_2 \times \Phi_{\mathrm{F\_PSII}} / \Phi_{\mathrm{F0\_PSII}}} \tag{17}$$

where m_1 and m_2 are 0.00561 and 0.00917, respectively, for SIF emission in the NIR region; Φ_{F_PSII} is the fluorescence yield in PSII at the steady-state condition; Φ_{F0_PSII} is the minimum fluorescence yield with a maximum proportion of open PSII reaction centers, assumed to be 0.02 (Liu et al., 2022). Φ_{F_PSII} is estimated as:

$$\Phi_{\mathrm{F\_PSII}} = \frac{K_{\mathrm{F}}}{K_{\mathrm{D}} + K_{\mathrm{F}} + \mathrm{NPQ}} \times (1 - \Phi_{\mathrm{PSII}}) \tag{18}$$

where K_D is the rate constant for constitutive heat loss; K_F is the rate constant for fluorescence emission. K_D and K_F are assumed to 0.9 and 0.1, respectively (Liu et al., 2022). In the NIR region, TOC SIF from PSII ($SIF_{TOC\_PSII}(\lambda)$, mW m^{-2} nm^{-1} sr^{-1}) can be estimated as: $SIF_{TOC\_PSII}(\lambda) = SIF_{TOC}(\lambda) \times f_{PSII}$.

Liu et al. (2022) showed that $f_C(\lambda)$, the ratio between SIF radiance at a given wavelength λ (nm) and the integral of SIF radiance over the full SIF spectrum (*640–850* nm), remains largely constant. Thus, $SIF_{TOC\_PSII}(\lambda)$ can be converted into TOC broadband PSII SIF (SIF_{TOC_FULL}, mW m^{-2} sr^{-1}): $SIF_{TOC\_FULL\_PSII} = SIF_{TOC\_PSII}(\lambda)/f_C(\lambda)$. We used the Soil Canopy Observation of Photosynthesis and Energy (SCOPE) model (version 1.73, van der Tol et al., 2009) to estimate $f_C(\lambda)$. Note that $SIF_{TOC\_FULL\_PSII}$ in the rMLR model has a unit of μmol m^{-2} s^{-1}, so one must also perform the unit conversion (Liu et al., 2022).

Zhang et al. (2019) showed that $f_{esc\_P\text{-}C}$ can be estimated as:

$$f_{\mathrm{esc\_P\text{-}C}} = 0.9 \times \frac{R\mathrm{veg}}{i_0 \times w} \tag{19}$$

where R_{veg} refers to the vegetation far-red reflectance at the same wavelength as $SIF_{TOC}(\lambda)$; i_0 represents the canopy interceptance and is determined by LAI, clumping index (CI) and solar zenith angle (SZA, °) (Chen and Leblanc, 2001); w represents the leaf albedo and is set to a constant value of unity (Yang and van der Tol, 2018; Zhang et al., 2019). R_{veg} is estimated as the difference between the observed reflectance at the same wavelength and observation direction as $SIF_{TOC}(\lambda)$ and the reflectance from the soil (Text S3).

2.5. Estimation of f_w and C_c

f_w is modeled using the empirical function (Wang et al., 2018; Wang and Leuning, 1998):

$$f_{\mathrm{w}} = \begin{cases} 0 & \theta_{\mathrm{S}} \le \theta_{\mathrm{W}} \\ \dfrac{\theta_{\mathrm{S}} - \theta_{\mathrm{W}}}{\theta_{\mathrm{F}} - \theta_{\mathrm{W}}} & \theta_{\mathrm{W}} < \theta_{\mathrm{S}} < \theta_{\mathrm{F}} \\ 1 & \theta_{\mathrm{S}} \ge \theta_{\mathrm{F}} \end{cases} \tag{20}$$

where θ_F and θ_W are the soil water content of the top 100 cm of soil at field capacity and at the wilting point, respectively; θ_S is the soil water content of the top 100 cm of soil.

An iterative process was used to estimate C_i (Fig. 1):

(1) calculate the initial C_i as a constant fraction of C_a:

$$C_{\mathrm{i}} = \begin{cases} 0.7 \times C_{\mathrm{a}} & \mathrm{C3} \\ 0.45 \times C_{\mathrm{a}} & \mathrm{C4} \end{cases} \tag{21}$$

where C_a is the ambient air CO_2 partial pressure (μbar) and the default ratio of C_i: C_a was set to 0.7 and 0.45 for C3 and C4, respectively (Wu et al., 2019).

(2) estimate Φ_{PSII}, NPQ, and f_{PSII} using the initial C_i and the other related inputs.
(3) calculate SIF-based A_{net} using the rMLR model.
(4) calculate G_c using the BWB-Leuning equation, and then convert it to canopy conductance to CO_2 (G_{c_co2}, mol m^{-2} s^{-1}) (Wang and Leuning, 1998).

$$G_{\mathrm{c\_co_2}} = 0.64 \times G_c \tag{22}$$

(5) obtain a new C_i based on the CO_2 diffusion model (Ju et al., 2006):

$$C_{\mathrm{i}} = C_{\mathrm{a}} - \frac{A_{\mathrm{net}}}{G_{\mathrm{c\_co_2}}} \tag{23}$$

(6) iterate Eqs. (21)–(23) until the estimated C_i is sufficiently stable, i.e. when the absolute difference in C_i between two successive iterations is <0.1 ppm. The G_c value from the final iteration is then used in the PM equation to estimate T.

3. Data

3.1. Input data for global T

3.1.1. Satellite data

We used SIF observations from the TROPOMI spectrometer (TROPOSIF) as our SIF data source. The Sentinel-5 Precursor that carries TROPOMI has a wide swath of 2600 km and a 16-day orbital period, giving it the ability to provide almost daily continuous global coverage with a high spatial resolution (7 × 3.5 km^2 at nadir). We collected

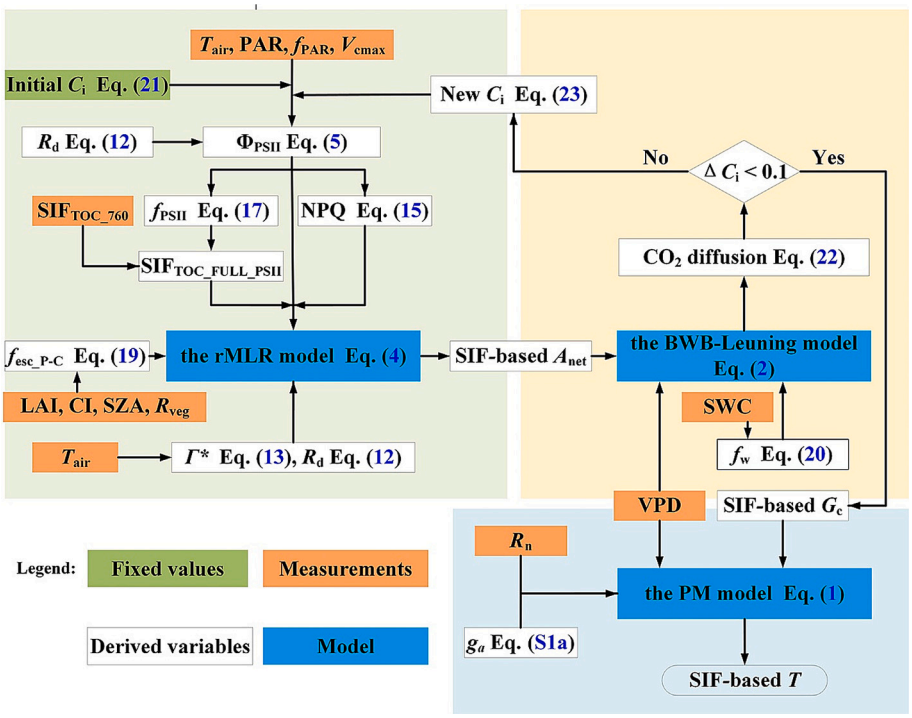

Fig. 1. Overview flowchart of the SIF-based ecosystem transpiration (T) model. The rMLR model is the reformulated mechanistic light response model; the BWB-Leuning equation is the Ball, Woodrow and Berry-Leuning equation; the PM equation is the Penman-Monteith model. The abbreviations and symbols are defined in Appendix A.

TROPOSIF L2B data from January 2019 to December 2020 (http://ftp.sron.nl/open-access-data-2/TROPOMI/tropomi/sif/v2.1/l2b/). We used daily average ungridded SIF retrievals from window 743–758 nm. To control the SIF data quality, we excluded SIF observations with cloud fractions larger than 0.2 from further analysis.

To implement the proposed model at the global scale, three MODIS data products were also required. LAI and f_{PAR} were acquired from the MODIS MCD15A3H v006 product with 4-day temporal and 500 m spatial resolutions (Myneni et al., 2015). The MODIS land cover type (MCD12C1 v006, Sulla-Menashe and Friedl, 2018) data product for 2019 which uses the International Geosphere-Biosphere Program classification scheme was used to determine the distribution of vegetation types with a spatial resolution of 0.05°.The CI data were sourced from a global foliage clumping index map derived from MODIS Bidirectional Reflectance Distribution Function (BRDF) products with a 500-m spatial resolution (He et al., 2012).

In this study, we used the global dataset of V_{cmax25} derived from leaf chlorophyll content (LCC, Chen et al., 2022). A two-step radiative transfer model was first employed to translate satellite reflectance in red, near infrared, and red-edge bands into global LCC time series (Croft et al., 2020). Using empirical relationships between LCC and V_{cmax} across various vegetation types (Luo et al., 2019), this LCC time series was then converted and aggregated into V_{cmax25} at a spatial resolution of 0.5°.

3.1.2. Meteorological data

The meteorological inputs used for the global SIF-based T simulation consist of T_{air}, R_n, SW and dew point temperature (T_d, °C). VPD, used in the PM equation (Eq. (1)) and the BWB-Leuning equation (Eq. (2)), was estimated from T_{air} and T_d (Wu et al., 2019). The hourly T_{air}, R_n, SW and T_d data were obtained from Modern-Era Retrospective Analysis for Research and Applications, Version 2 (MERRA-2) (https://disc.gsfc.nasa.gov, Gelaro et al., 2017), with a spatial resolution of 0.625° longitude × 0.5° latitude. The hourly values of these three meteorological variables were converted into daytime averages to match the SIF data used in this study.

3.1.3. Soil data

The required θ_F and θ_W data were estimated from the database of global soil hydraulic properties (https://doi.pangaea.de/10.1594/PANGAEA.870605) developed by Montzka et al. (2017). This database provides a variety of key soil hydraulic parameters at seven predefined depths (0, 5, 15, 30, 60, 100, and 200 cm) at a resolution of 0.25°. The weighted averages of the top 100 cm were used in this study.

We collected hourly volumetric soil water content (SWC) from the European Center for Medium-Range Weather Forecasts (ECMWF), the fifth generation of European Reanalysis (ERA5, hereafter ERA5-Land). The ERA5-Land is a reanalysis dataset providing high-resolution (~9 km) information on hourly surface variables between 1950 and the near present (Ma et al., 2022). In the ERA5-Land data, simulated SWC is available at four depths (0, 7, 28, 100, and 289 cm). In this study, we used the depth-weighted mean of daytime SWC across the top three soil layers (0–100 cm).

3.1.4. Pre-processing global input data

To run the proposed model on a global scale, it is necessary to integrate all the aforementioned datasets. For T_{air}, T_d, R_n, PAR, and SWC, we aggregated the hourly values of these variables into daytime averages to match the SIF data used in this study. The daytime hours are calculated based on latitude and the day of the year. For 4-day composite LAI and f_{PAR}, we used a linear temporal interpolation to temporally rescale them into daily estimates. The land cover, CI, V_{cmax25}, θ_F and θ_W data are assumed unchanged during the study period. Note that TROPOMI SIF measurements (also R_{veg} and SZA) are ungridded, the values of the gridded datasets were extracted according to the locations of data points in TROPOMI SIF measurements. For display purposes, the simulated T estimates were gridded to a spatial resolution of 5 × 5 km^2, and then composited over 8 days using the GriddingMachine tool (Wang et al., 2022b). The detailed data processing workflow is shown in Fig. S1.

3.2. Site description and eddy covariance flux tower data

To evaluate the performance of the proposed SIF-based model at the site scale, we collected turbulent fluxes of latent heat (λE) from AmeriFlux (27 sites), CarboEurope (1 sites), and OzFlux (3 sites) based on the availability of data during the period January 2019 to December 2020. The variations in λE are dominated by canopy T when evaporation from soil and intercepted water on leaves is minimal. Thus, the following criteria were applied to select the λE measurements: (1) data with precipitation events (> 1 mm/h) as well as the subsequent 48 h were excluded to reduce the negative impact due to evaporation from soil and plant canopy evaporation, and (2) data with LAI > 1.0 m^2 m^{-2} were selected for each site. Also, at each site, the dominant land cover within a 7 km radius had to account for >70% of the area.

Half-hourly or hourly values of λE at each site were then converted to daytime values (T_{EC}, mm day^{-1}). For simplicity, we combined certain classes according to the International Geosphere-Biosphere Program (IGBP) land-cover classification: croplands and croplands/natural vegetation mosaics were combined as croplands (Zhang et al., 2019). The final result of the process was 31 sites covering ten different IGBP vegetation types: croplands (CRO, five sites), closed shrubland (CS, three sites), deciduous broadleaf forest (DBF, three sites), evergreen broadleaf forest (EBF, three sites), evergreen needleleaf forest (ENF, four sites), grasslands (GRA, three sites), mixed forest (MF, two sites), open shrubland (OS, five sites), savannas (S, two sites), and woody savannas (WS, one sites). Detailed information on these sites is provided in Table 1. The proposed T estimation model, forced with the satellite inputs and the gridded meteorological data, was evaluated against T_{EC} at these selected sites. To do this, ungridded T estimates from the global simulation (T_{SIF}, mm day^{-1}) were averaged over the surrounding 7 km^2 at each site.

4. Results

4.1. T validation at the site scale

The correlation coefficient (R^2) for all sites is 0.75, the root mean square error (RMSE) is 1.23 mm day^{-1} and the relative root mean square error (rRMSE) is 10.27%. The model demonstrated particularly strong capabilities in estimating canopy transpiration in most forest types. In deciduous broadleaf forests, it explained >75% of the variance in T_{EC} (R^2 = 0.77, RMSE = 1.18 mm day^{-1}, and rRMSE = 11.98%, Fig. 2c). Similarly, in evergreen broadleaf forests and mixed forests, it achieved a high level of accuracy, accounting for 72% of variability in the daily T_{EC} time series (RMSE = 0.71 mm day^{-1}, rRMSE = 13.64%, Fig. 2d and RMSE = 1.42 mm day^{-1}, rRMSE = 20.40%, Fig. 2g). The correlation between T_{SIF} and T_{EC} was also strong in evergreen needleleaf forests (RMSE = 1.06 mm day^{-1}, and rRMSE = 12.69%, Fig. 2e), with R^2 = 0.64. Correlations between T_{SIF} and T_{EC} remained strong in croplands (R^2 = 0.68, RMSE = 1.85 mm day^{-1}, and rRMSE = 15.40%, Fig. 2a) and grasslands (R^2 = 0.72, RMSE = 1.50 mm day^{-1}, and rRMSE = 13.22%, Fig. 2f), suggesting that homogeneous canopies tend to enhance the performance of the proposed model.

At closed shrubland sites and savannas, the model explained 54% (RMSE = 1.49 mm day^{-1}, and rRMSE = 16.05%, Fig. 2b) and 55% (RMSE = 0.62 mm day^{-1}, and rRMSE = 13.72%, Fig. 2i) of the variance in T_{EC} variability, respectively. However, the accuracy of T_{SIF} generally showed a decreasing trend in ecosystems such as open shrubland (RMSE = 0.54 mm day^{-1}, and rRMSE = 13.12%, Fig. 2h) and woody savannas (RMSE = 0.58 mm day^{-1}, and rRMSE = 19.37%, Fig. 2j), T_{SIF} explained around 51% of the variance in daily T_{EC}.

4.2. Global G_c and T estimates

Using the TROPOMI ungridded daily SIF data and the other required

Table 1
Information for the flux-tower sites used in this study. From left to right: station name; International Geosphere–Biosphere International Programme (IGBP) classification; latitude; longitude; dominant land cover percentage, references. (CRO, croplands; CS, closed shrubland; DBF, deciduous broadleaf forest; EBF, evergreen broadleaf forest; ENF, evergreen needleleaf forest; GRA, grasslands; MF, mixed forest; OS, open shrubland; S, savannas; and WS, woody savannas).

Site ID	IGBP	Latitude (°)	Longitude (°)	Percentage (%)	Reference
US-CF2	CRO	46.7840	−117.0908	0.95	Chu et al. (2021)
US-CF4	CRO	46.7518	−117.1285	0.92	Chu et al. (2021)
US-CS3	CRO	44.1394	−89.5727	0.85	Jaafar et al. (2022)
US-CS4	CRO	44.1597	−89.5475	0.87	Wu et al. (2022)
US-Ro6	CRO	44.6946	−93.0578	0.95	Chu et al. (2021)
US-Rls	CS	43.1439	−116.7356	1.00	Goodwell et al. (2018)
US-Rms	CS	43.0645	−116.7486	1.00	Goodwell et al. (2018)
US-Rwf	CS	43.1207	−116.7231	1.00	Flerchinger and Seyfried (2014)
US-xBL	DBF	39.0603	−78.0716	0.74	Metzger et al. (2019)
US-xML	DBF	37.3783	−80.5248	1.00	Metzger et al. (2019)
US-xSC	DBF	38.8929	−78.1395	0.80	Metzger et al. (2019)
AU-GWW	EBF	−30.1914	120.6542	0.70	Prober et al. (2011)
AU-Robson	EBF	−17.1175	145.6301	0.89	Maes et al. (2020)
AU-Warra	EBF	−43.0950	146.6545	0.91	Beringer et al. (2022)
US-Ho1	ENF	45.2041	−68.7402	1.00	Fernandez et al. (1993)
US-NR1	ENF	40.0329	−105.5464	0.85	Reich et al. (1998)
US-Vcm	ENF	35.8884	−106.5321	0.85	Biederman et al. (2016)
US-xSB	ENF	29.6893	−81.9934	1.00	Metzger et al. (2019)
US-Ro4	GRA	44.6781	−93.0723	0.99	Zhang et al. (2020)
US-xDC	GRA	47.1617	−99.1066	1.00	Metzger et al. (2019)
US-xWD	GRA	47.1282	−99.2414	1.00	Chu et al. (2021)
US-Syv	MF	46.2420	−89.3477	0.71	Desai (2010)
US-xUN	MF	46.2339	−89.5373	0.93	Metzger et al. (2019)
US-Jo2	OS	32.5849	−106.6032	0.91	Li and Xiao (2022)
US-Mpj	OS	34.4384	−106.2377	1.00	Wood (2022)
US-Rws	OS	43.1675	−116.7132	1.00	Goodwell et al. (2018)
US-xJR	OS	32.5907	−106.8425	1.00	Metzger et al. (2019)
US-xSR	OS	31.9107	−110.8355	0.94	Metzger et al. (2019)
US-Wjs	S	34.4255	−105.8615	0.93	Wang et al. (2022a)
ES-Abr	S	38.7018	−6.7859	0.90	El-Madany et al. (2020)
US-SRM	WS	31.8214	−110.8661	0.88	Goodwell et al. (2018)

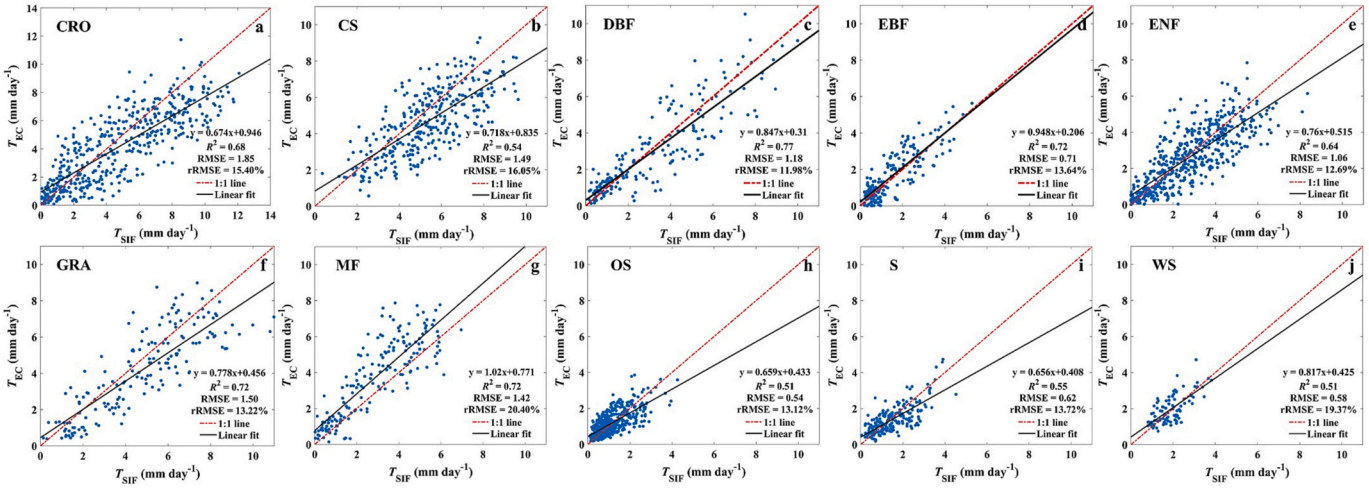

Fig. 2. Comparison between the daily observed and estimated transpiration from TROPOMI SIF (T_{EC} versus T_{SIF}, mm day^{-1}). Figure shows the linear regression between the modeled and observed estimates for (a) CRO, croplands; (b) CS, closed shrubland; (c) DBF, deciduous broadleaf forest; (d) EBF, evergreen broadleaf forest; (e) ENF, evergreen needleleaf forest; (f) GRA, grasslands; (g) MF, mixed forest; (h) OS, open shrubland; (i) S, savannas; and (j) WS, woody savannas. R^2 is the coefficient of determination, RMSE is the root-mean-square error (mm day^{-1}), and rRMSE is the relative root-mean-square error (%). The red dash-dotted lines are the 1:1 lines, and the black lines represent the linear regressions between the observed and predicted values. (For interpretation of the references to color in this figure legend, the reader is referred to the web version of this article.)

Table 2
Mean annual and seasonal SIF-based transpiration (T_{SIF}, mm yr^{-1}) and canopy conductance for water vapor (G_{c_SIF}, m s^{-1}) across different vegetation types during 2019–2020. IGBP, the land-cover classification of the International Geosphere-Biosphere Program; CRO, croplands; CS, closed shrubland; DBF, deciduous broadleaf forest; EBF, evergreen broadleaf forest; ENF, evergreen needleleaf forest; GRA, grasslands; MF, mixed forest; OS, open shrubland; S, savannas; and WS, woody savannas; MAM, March–May; JJA, June–August; SON, September–November; DJF, December–February.

IGBP	Mean annual	MAM	JJA	SON	DJF
CRO	390.62 (0.0061)	78.68 (0.0057)	151.44 (0.0071)	62.22 (0.0054)	98.28 (0.0046)
CS	248.24 (0.0065)	47.67 (0.0058)	100.00 (0.0077)	41.34 (0.0054)	59.22 (0.0055)
DBF	251.52 (0.0067)	48.40 (0.0061)	87.27 (0.0076)	46.36 (0.0061)	69.81 (0.0064)
EBF	311.10 (0.0082)	66.36 (0.0085)	90.32 (0.0079)	74.34 (0.0081)	80.07 (0.0086)
ENF	169.65 (0.0062)	20.79 (0.0053)	98.42 (0.0073)	31.53 (0.0049)	18.91 (0.0033)
GRA	287.41 (0.0047)	61.40 (0.0049)	94.88 (0.0051)	51.74 (0.0043)	79.38 (0.0046)
MF	214.06 (0.0066)	37.56 (0.0056)	92.09 (0.0081)	34.63 (0.0056)	49.79 (0.0050)
OS	236.51 (0.0058)	47.89 (0.0055)	86.72 (0.0069)	38.49 (0.0051)	63.42 (0.0053)
S	296.44 (0.0055)	67.96 (0.0054)	86.30 (0.0060)	52.25 (0.0048)	89.93 (0.0054)
WS	231.31 (0.0057)	45.85 (0.0054)	79.54 (0.0065)	35.37 (0.0047)	70.54 (0.0056)
Global	278.45 (0.0059)	58.11 (0.0056)	96.26 (0.0064)	48.46 (0.0052)	75.61 (0.0057)

inputs (Section 3), we implemented the proposed *T* estimation model to obtain global G_{c_SIF} and T_{SIF} over the vegetated land surface at a daily time step for the period 2019–2020. The forest ecosystems had higher canopy conductance (Table 2). For instance, the values of mean annual G_{c_SIF} in evergreen broadleaf forest (0.0082 m s^{-1}) and deciduous broadleaf forest (0.0067 m s^{-1}) were higher than in savannas (0.0055 m s^{-1}) and grasslands (0.0047 m s^{-1}). The southern hemispheric tropics generally showed high values of G_{c_SIF}: tropical and subtropical forests in the northwest Amazon, central Africa, and southeast Asia had an average annual G_{c_SIF} of approximately 0.0092 m s^{-1}, 0.0085 m s^{-1}, and 0.0125 m s^{-1}, respectively (Fig. 3a). In contrast, southeast Amazon, eastern and southern Africa, and northern and eastern Australia — all areas dominated by (woody) savannas and grasslands — had lower values of G_{c_SIF}, ranging from 0.0009 m s^{-1} to 0.0035 m s^{-1} (Fig. 3a). In the Northern Hemisphere, G_{c_SIF} presented a generally increasing trend with increasing latitude. Mean annual G_{c_SIF} values in China and India, for example, were mostly below 0.0060 m s^{-1}, whereas those over large areas of Europe and Siberia were >0.0078 m s^{-1} (Fig. 3a).

In most cases, an increase in air temperature enhances atmospheric dryness (i.e., VPD). Increased VPD typically causes stomatal closure to prevent excess water loss, however, the plant photosynthesis rate and thus canopy conductance may increase with rising air temperature until a given threshold. Fu et al. (2022) showed that the response of plant transpiration to increasing VPD depended on soil dryness (i.e., SWC). Using partial correlation analysis, we next assess the relative roles (Pearson correlation coefficient, *r*) of VPD and SWC in determining the impact of dryness stress on G_{c_SIF} and T_{SIF}. *P*-values <0.05 are considered significant. To filter out days when transpiration could be significantly influenced by other meteorological factors (e.g., incoming shortwave radiation), we focused on the growing season and selected days when SWC and VPD were most likely to be the dominant controllers of ecosystem transpiration. Following previous research (Anderegg et al., 2018; Liu et al., 2020; Sulman et al., 2016), we carried out partial correlation analyses under the following conditions: (1) the daily average temperature was >15 °C; (2) sufficient atmospheric water demand existed to drive water fluxes, as evidenced by a daily average VPD exceeding 0.5 kPa; (3) there was high solar radiation, evidenced by a daily average photosynthetic photon flux density surpassing 500 μmol m^{-2} s^{-1}.

Overall, G_{c_SIF} exhibited a negative correlation with VPD during the study period, prevailing over 88.98% of vegetated areas (44.74% with a significant negative correlation, Fig. 3b). The response of G_{c_SIF} to increasing VPD becomes less negative (increasing *r*) under lower VPD values, and can even become positive when VPD is below a certain threshold. For example, G_{c_SIF} over 95.34% of vegetated land south of 35° North was negatively correlated with VPD (68.17% significant,

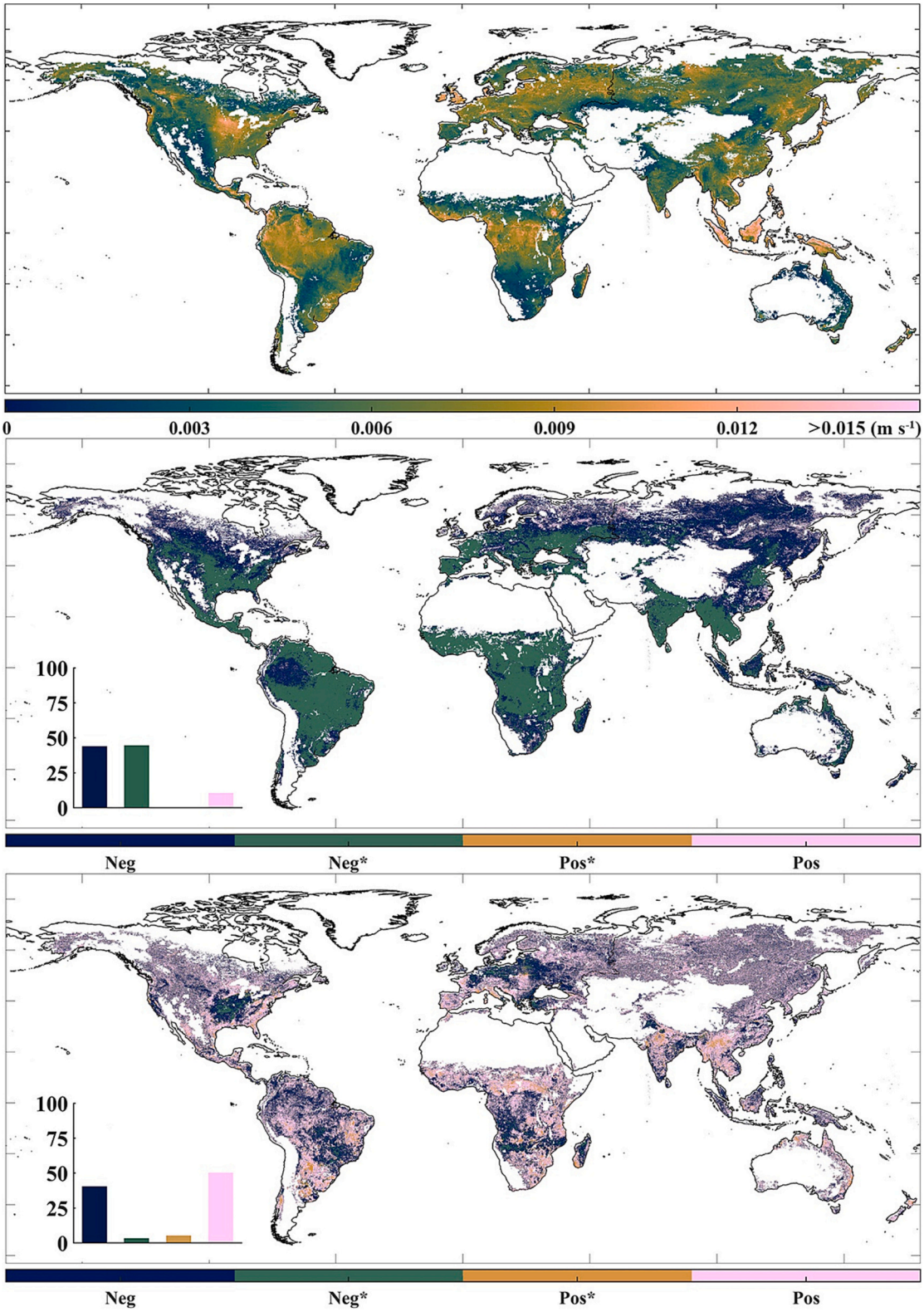

Fig. 3. Spatial distribution of mean canopy conductance for water vapor (G_{c_SIF}, m s^{-1}) estimated by the proposed model over the period 2019–2020 (a), and spatial patterns of partial correlations between G_{c_SIF} and atmospheric vapor pressure deficit (VPD, kPa) (b)/soil water content (SWC, %) of the top 100 cm soil layer (c) on a daily basis for the same period. The insets in (b) to (c) show the relative frequency (%) distribution of negative correlations (Neg; blue), significant negative correlations (Neg*; $P < 0.05$; cyan), significant positive correlations (Pos*; $P < 0.05$; yellow), and positive correlations (Pos; red). Vegetated regions (using IGBP land cover classifications) are shown in color, while regions in white are barren or sparsely vegetated areas and non-vegetated areas, including water bodies, snow, desert and ice, and urban areas. (For interpretation of the references to color in this figure legend, the reader is referred to the web version of this article.)

Fig. 3b, Fig. S4), while in high northern latitudes (> 45° N), G_{c_SIF} was significantly reduced due to atmospheric drying over only 16.09% of vegetated areas (Fig. 3b, Fig. S5). Grid cells with positive correlations of G_{c_SIF} to SWC occupied 55.79% of vegetated areas, while those with negative correlations made up 44.21%. In both cases these grid cells were widely distributed globally (Fig. 3c). However, the correlations between G_{c_SIF} and SWC were mostly insignificant, with only 5.34% of them having a significant positive correlation and only 3.51% a significant negative one (Fig. 3c), suggesting that SWC has a weak impact on G_{c_SIF} across a large range of soil water deficits.

We found that G_{c_SIF} tended to significantly increase in response to increasing SWC under low SWC conditions (Fig. S6). For example, by the end of the dry season and during the transition to the wet season across the Amazon basin (dry soils), the onset of rainfall (increasing SWC) contributes to a rapid increase in regional vegetation productivity and G_{c_SIF} (Restrepo-Coupe et al., 2013), leading to a positive response of G_{c_SIF} to SWC. On the other hand, in predominantly humid or sub-humid regions, many vegetated areas exhibited a significant negative correlation between G_{c_SIF} and VPD. In these regions, a slight reduction in SWC can lead to increased nitrogen uptake, subsequently enhancing photosynthesis and canopy conductance (Sardans et al., 2017).

Averaged over 2019–2020, the mean annual T_{SIF} over the part of the global vegetated land surface with valid data was 278.45 mm yr^{-1} (Fig. 4a, Table 2), accounting for 32.36% of precipitation during this 2-year period. Ecosystem transpiration was found to differ considerably among the different vegetation types (Table 2): croplands had the highest mean annual T_{SIF} of 390.62 mm yr^{-1}, followed by evergreen broadleaf forest (311.10 mm yr^{-1}), while evergreen needleleaf forest had the lowest T_{SIF} (169.65 mm yr^{-1}). Due to the rapid increase in available energy and vegetation growth during the summer, strong seasonality in T_{SIF} was found in some vegetation types, particularly those located mainly in mid- and high latitude regions. For instance, the values of T_{SIF} in evergreen needleleaf forest were much higher in the summer months (June, July and August), contributing >55% of its annual total T_{SIF} (Table 2). In contrast, in tropical vegetation, T_{SIF} showed little seasonal variation: evergreen broadleaf forest, for example, had almost the same T_{SIF} in each season (Table 2).

Annual T_{SIF} generally decreased with increasing latitude in mid- and high latitudes (Fig. 4a): forests in subtropical and warm temperate zones had high values of mean annual T_{SIF} (> 700 mm yr^{-1}); forests in cool temperate and subarctic zones had a much shorter growing season, resulting in low estimates of annual T_{SIF} (< 200 mm yr^{-1}, Fig. 4a), despite having high values of G_{c_SIF} (Fig. 3a). Somewhat counterintuitively, humid tropical rainforests, in equatorial Amazonia, Central Africa, and Southeast Asia, showed relative moderate annual T_{SIF} (about 400 mm yr^{-1}, Fig. 4a), despite these forests having a great availability of liquid water in the forest canopy due to their large LAI and high rainfall. One explanation for the moderate values is that evaporation of canopy intercepted water leads to declines in within-canopy vapor pressure deficit and canopy temperature, thus reducing ecosystem water loss through transpiration (Dawson and Goldsmith, 2018).

T_{SIF} exhibited a positive correlation with increasing VPD over approximately 80% of vegetated areas (26.68% significant, Fig. 4b). Approximately 19% of the vegetated surface showed a negative correlation between T_{SIF} and VPD, but <3% of these correlations were significant (Fig. 4b). Considering that G_{c_SIF} significantly decreased due to elevated VPD over 44.74% of vegetated land (Fig. 3b), these results confirm that, globally, the increase in atmospheric demand for water tended to overwhelm the plants' ability to conserve water during the study period.

The correlation between T_{SIF} and SWC was statistically insignificant over 92.01% of vegetated areas (Fig. 4c). Only 3.13% of global vegetated land, mainly scattered in southeastern North America, southern Brazil, and western Europe, showed significant negative correlations (Fig. 4c). T_{SIF} had a significant positive response to SWC variation across 4.86% of vegetated areas, which were mainly in northern South America, southeastern South America, and west and central Africa (Fig. 4c). Although a weak constraint of SWC changes on T_{SIF} was observed, a decline in SWC tended to weaken the VPD-T_{SIF} relationship: the correlations between T_{SIF} and VPD were significantly positive over 34.35% of vegetated grid cells, with $f_w = 1.0$ (Eq. (20)), while they were significantly positively correlated with each other over only 15.54% of vegetated grid cells, with $f_w < 0.5$ (Table S2).

4.3. Comparison of T_{SIF}, T_{MODIS} and T_{GLEAM}

Next, we investigated the main factors causing the deviation between T_{SIF}, T_{MODIS} and T_{GLEAM} (the validation results of T_{MODIS} and T_{GLEAM} at the mentioned sites are provided in Supplementary Material (Text S4 - S5). First, the spatial distribution of the mean daily difference between T_{MODIS} and T_{SIF} (T_{DM}: T_{MODIS} - T_{SIF}, mm day^{-1}), T_{GLEAM} and T_{SIF} (T_{DG}: T_{GLEAM} - T_{SIF}, mm day^{-1}) during 2019–2020 was determined. To ensure the correct interpretation of T_{DM} and T_{DG}, we avoid temporal interpolation: T_{DM} and T_{DG} was estimated only when T_{SIF}, T_{MODIS} and T_{GLEAM} all had valid values. Overall, T_{SIF} generally agrees well with T_{MODIS}: T_{DM} varies in a small range between −0.5 and 0.5 mm day^{-1} on 42.9% of the vegetated grid cells meeting the selection criteria (Fig. 5a). In 29.03% of these vegetated areas, T_{SIF} records higher values than T_{MODIS}, resulting in a negative T_{DM}. However, of these areas, only 28.39% have a T_{DM} less than −1.0 mm day^{-1} (Fig. 5a), indicating that the overestimation of the proposed model compared to the MODIS T estimation model is limited.

Nearly 70% (70.97%) of global vegetated areas have a positive T_{DM}. Two large peaks of positive T_{DM} values (> 3.0 mm day^{-1}) can be identified on the Indo-China Peninsula and the southern margin of the Amazon Basin (Fig. 5a). In these two regions, T_{MODIS} is noticeably higher than T_{SIF} during the dry season, accounting for the annual positive T_{DM} (Fig. S7c, e); conversely, during the wet season with high F_{wet}, T_{MODIS} is smaller than T_{SIF} in these regions (Fig. S7a, g). Another hotspot of positive T_{DM} is the boreal evergreen forest region (> 60° N), spanning vast parts of Canada and Russia (Fig. 5a). In this region, without a clear separation between dry and wet seasons, the overestimation of T_{MODIS} over T_{SIF} becomes more pronounced as LAI increases during the summer (Fig. S7c, e).

T_{SIF} deviates more from T_{GLEAM}: T_{DG} varies between −0.5 and 0.5 mm day^{-1} on 28.85% of the vegetated grid cells (Fig. 5b). The GLEAM model employs lightning data to infer rainfall events (Miralles et al., 2010; Zheng and Jia, 2020). However, lightning and rainfall do not always occur simultaneously. Consequently, the GLEAM model tends to underestimate rainfall, resulting in reduced estimates of canopy interception loss in regions with dense vegetation and heavy rainfall. This, in turn, causes an overestimation of transpiration in such areas (Eq. S2c in text S2). This pattern is evident in the Amazon basin, Congo basin, and Southeast Asia, where expansive areas exhibit T_{DG} > 3 mm day^{-1} (Fig. 5b). Particularly, in regions with distinct rainy and dry seasons, such as the southern regions of the Amazon and Congo basins, T_{DG} displays more positive values in the wet season (Fig. S7b, h), compared to the dry season (Fig. S7d, f).

The GLEAM model does not include irrigation (Martens et al., 2017). As a result, it overlooks the increased transpiration due to irrigation in many agricultural areas, leading to an underestimation of transpiration. This explains why key agricultural regions globally, like the American Midwest and the plains of North and Northeast China, display large areas with negative T_{DG} (Fig. 5b), particularly during summer when irrigation practices are more frequent (Fig. S7d).

The GLEAM model might not fully capture the transpiration in energy-limited areas (Miralles et al., 2016), which elucidates the expansive regions with negative T_{DG} seen in Siberia and northern Canada (Fig. 5b). During summer, as energy-limited areas are exposed to increased radiation, the underestimation of T_{GLEAM} diminishes, making it more comparable to T_{SIF} (Fig. S7d). Conversely, the underestimation of T_{GLEAM} could be more pronounced in spring and autumn, leading to even more negative T_{DG} values in these areas during these seasons

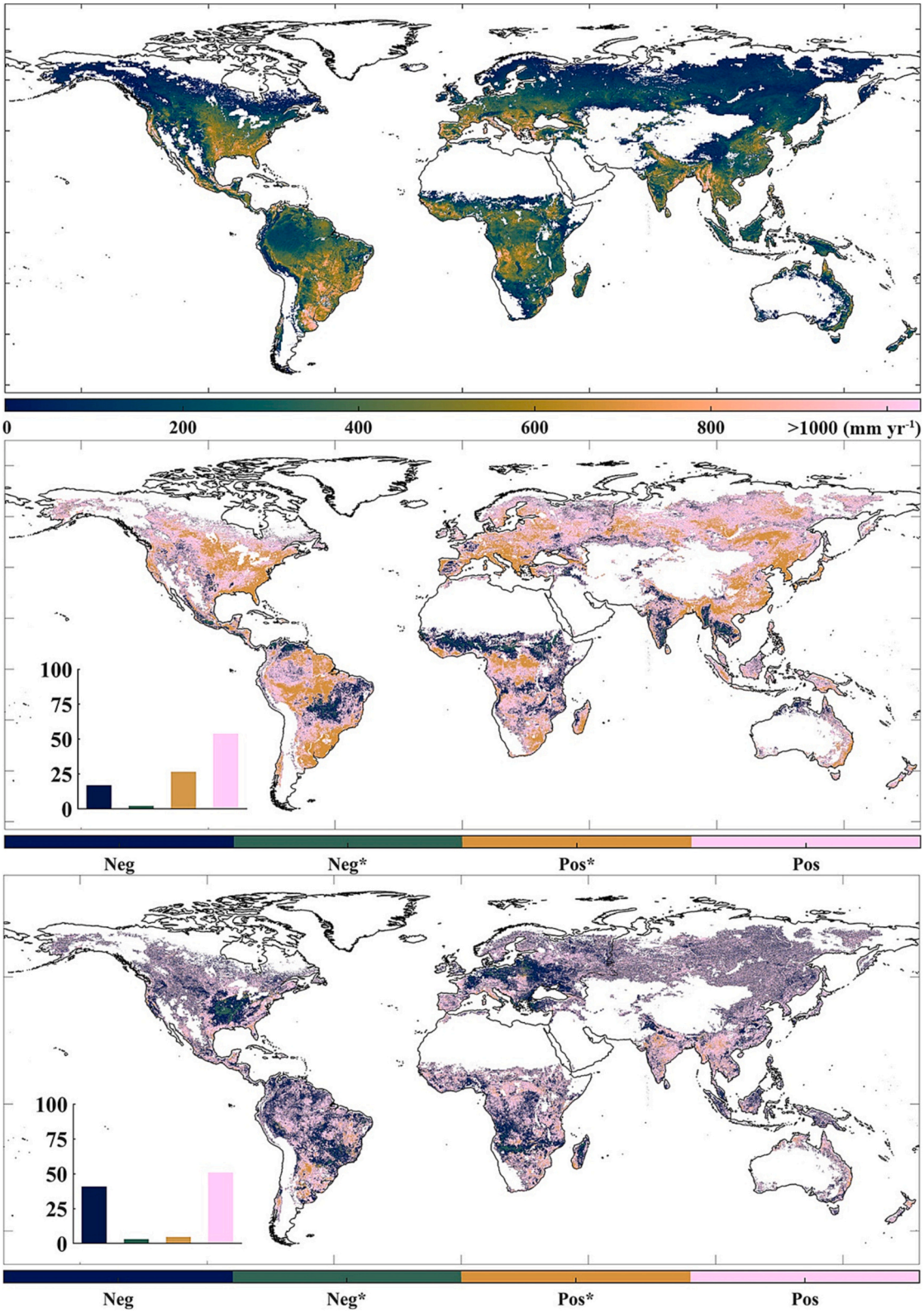

Fig. 4. Spatial distribution of mean annual ecosystem transpiration estimated by the proposed model (T_{SIF}, mm yr^{-1}) over the period 2019–2020 (a), and spatial patterns of correlations between T_{SIF} and atmospheric vapor pressure deficit (VPD, kPa) (b), soil water content (SWC, %) of the top 100 cm soil layer (c) on a daily basis for the same period. The insets in (b) and (c) show the relative frequency (%) distribution of negative correlations (Neg; blue), significant negative correlations (Neg*; $P < 0.05$; cyan), significant positive correlations (Pos*; $P < 0.05$; yellow), and positive correlations (Pos; red). Vegetated regions (using IGBP land cover classifications) are shown in color, while regions in white are barren or sparsely vegetated areas and non-vegetated areas, including water bodies, snow, desert and ice, and urban areas. (For interpretation of the references to color in this figure legend, the reader is referred to the web version of this article.)

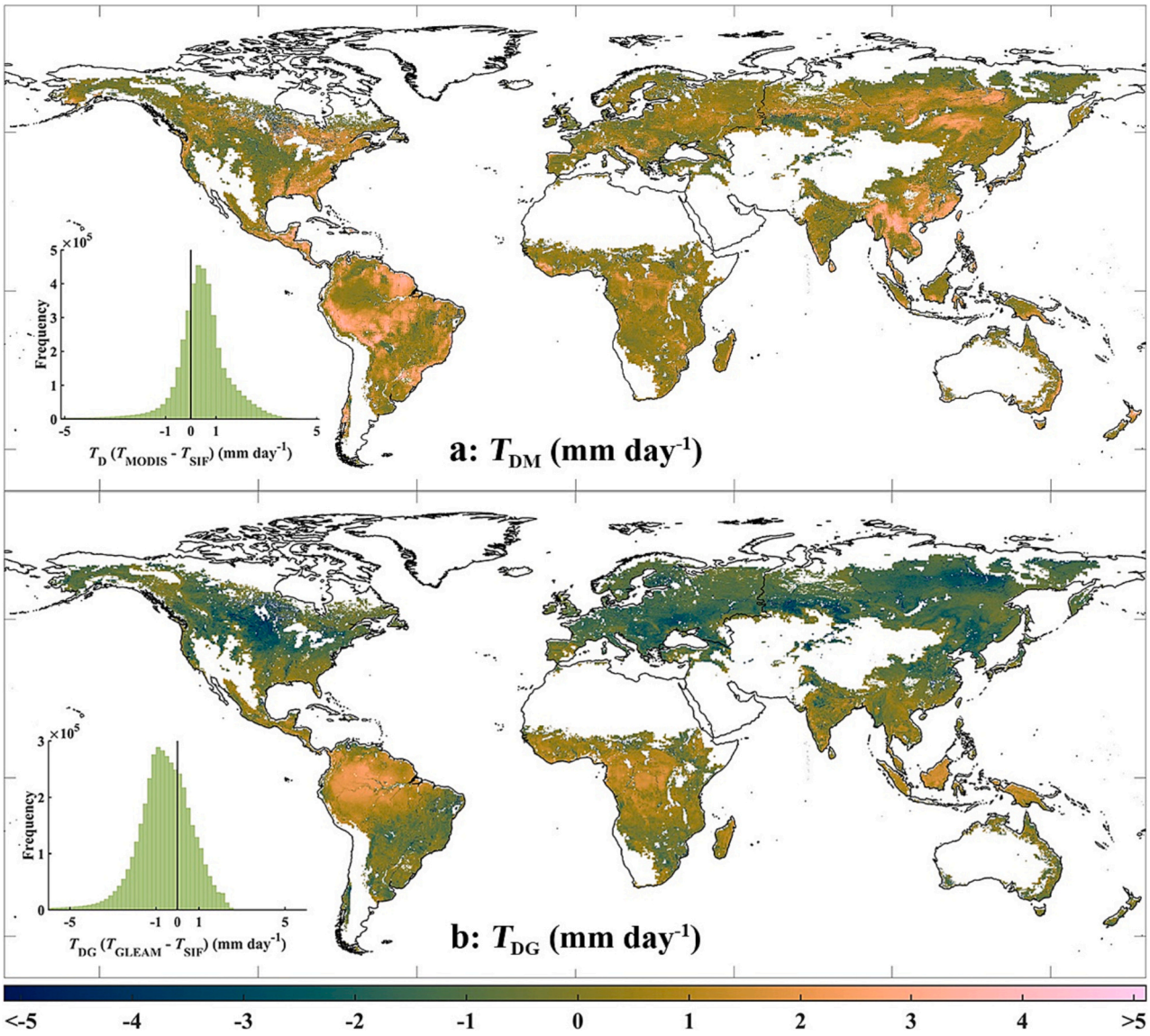

Fig. 5. Spatial distribution of the difference in mean daily ecosystem transpiration estimated by the MODIS model (T_{MODIS}, mm day^{-1}) and the proposed model (T_{SIF}, mm day^{-1}) (a: T_{DM}: T_{MODIS} - T_{SIF}, mm day^{-1}), the difference between transpiration estimated by GLEAM (T_{GLEAM}, mm day^{-1}) and T_{SIF} (b: T_{DG}: T_{GLEAM} - T_{SIF}, mm day^{-1}) over the period 2019–2020. The inset panel shows the histogram of T_{DM} and T_{DG}. Vegetated regions (using MCD12C1 land cover type 1) are shown in color, while white regions are barren or sparsely vegetated areas and non-vegetated areas, including water bodies, snow, desert and ice, and urban areas.

(Fig. S7b, f).

The spatial distribution of T_{DM} suggests that the overestimation of the MODIS T model, with respect to the proposed model, increases as LAI increases, but tends to decrease with increasing F_{wet}. In contrast, the overestimation of T_{GLEAM} over T_{SIF} increases not only with the increase of LAI but also with the increase of rainfall. To examine how T_{DM} and T_{DG} varies with LAI and F_{wet} (a proxy for rainfall, Eq. (3b)), T_{DM}, T_{DG} and LAI were sorted into 7 bins according to the 0-10th, 10-20th, …, and 60-70th percentiles of F_{wet}. Within each F_{wet} bin, T_{DM} and T_{DG} was divided into four groups based on LAI values: (1) low: 0.0 < LAI < 1.5, (2) low and intermediate: 1.5 < LAI < 2.0; (3) intermediate: 2.0 < LAI < 3.5, and (4) high: 3.5 < LAI < 6.0.

As illustrated in Fig. 6a, most of T_{DM} values typically vary between −1.0 and 1.0 mm day^{-1} when LAI < 3.5 m^2 m^{-2}. Further, T_{DM} has an increasing trend with increasing LAI in low F_{wet} conditions. For example, in the bin with the lowest F_{wet} (< 0.1), the mean T_{DM} is −0.67 mm day^{-1} in the low LAI group, while it increases to −0.12 mm day^{-1} and 0.36 mm day^{-1} in the low and intermediate, and intermediate LAI groups, respectively (Fig. 6a). Further, the mean T_{DM} is enhanced under high LAI values, reaching a maximum of 2.42 mm day^{-1} when F_{wet} < 0.1 (Fig. 6a). However, the differences between T_{SIF} and T_{MODIS} tend towards to zero with increasing F_{wet}: the maximum of the mean T_{DM} declines to <1 mm day^{-1} in the bin with F_{wet} in the range of 0.4–0.5, and the variations in T_{DM} are insensitive to LAI when F_{wet} > 0.5 (Fig. 6a). This strong dependence of T_{DM} on canopy structure, as characterized by LAI, suggests that the conductance upscaling scheme from leaf to canopy is a major reason for the difference between T_{SIF} and T_{MODIS}. Note that the MODIS T estimation model uses LAI to parameterize canopy processes: all leaves in the canopy are assumed to have the same leaf stomatal conductance, and canopy conductance is simply obtained by upscaling leaf stomatal conductance by LAI. As a consequence, T_{DM} shows a positive correlation with LAI (see the Discussion section).

Conversely, as F_{wet} increases, T_{DG} displays a rising trend when LAI exceeds 2.0 m^2 m^{-2} (Fig. 6b). For example, with an increase in F_{wet} from 0.1 to 0.7, the mean T_{DG} in the high LAI group increases from −0.43 mm day^{-1} to 2.11 mm day^{-1}. This pattern aligns with the overestimation of T_{GLEAM} in relation to T_{SIF} observed in areas characterized by complex canopies and significant rainfall (Fig. 5b). The majority of mean T_{DG}

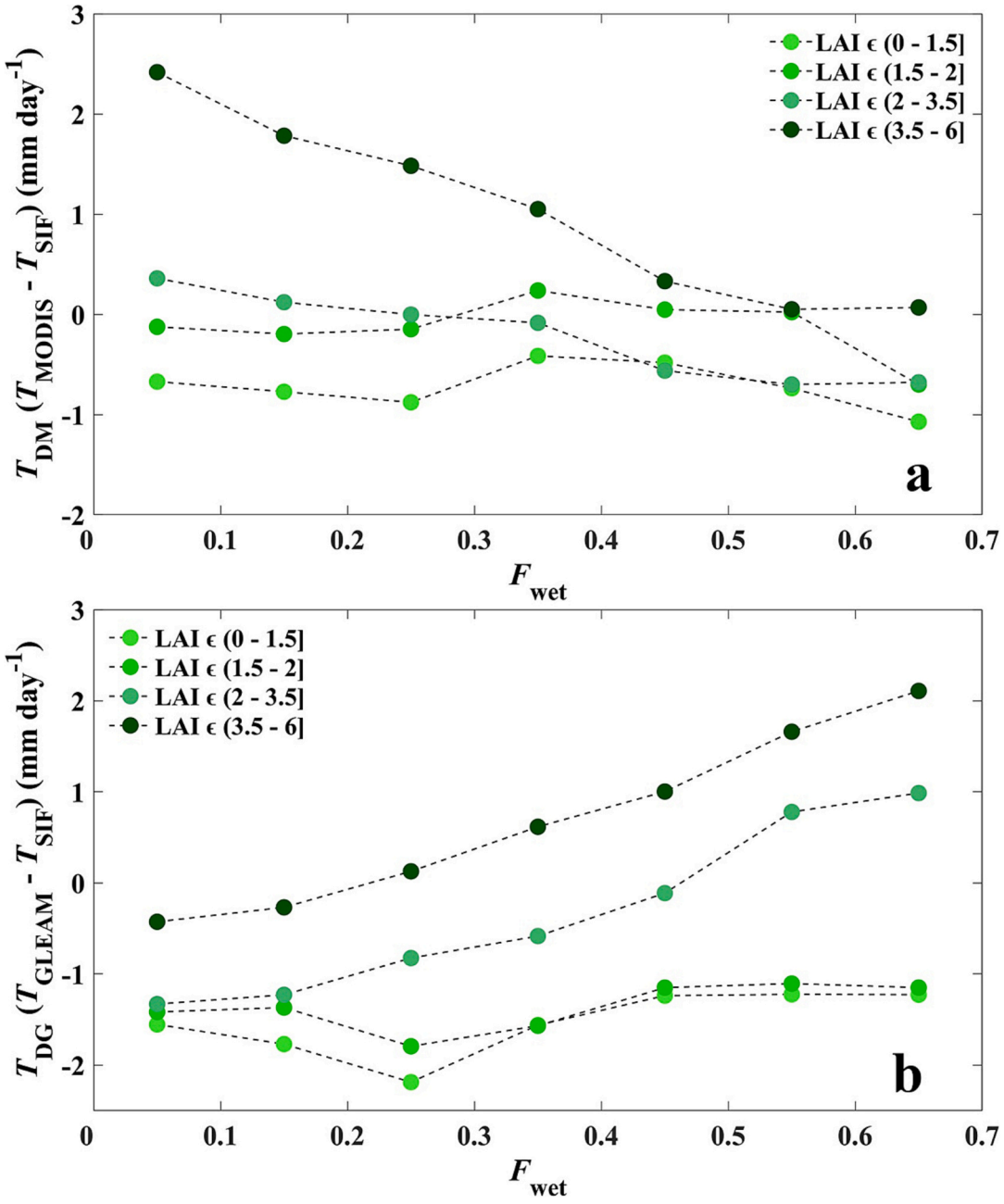

Fig. 6. The variation of T_{DM} and T_{DG} across leaf area index (LAI, m^2 m^{-2}) gradients in water cover fraction (F_{wet}, %) bins. T_{DM} and T_{DG} represents the difference between mean daily ecosystem transpiration estimated by the MODIS model (T_{MODIS}, mm day^{-1}) and the proposed model (T_{SIF}, mm day^{-1}), the difference between transpiration estimated by GLEAM (T_{GLEAM}, mm day^{-1}) and T_{SIF} over the period 2019–2020 (a: T_{DM}: T_{MODIS} - T_{SIF}, mm day^{-1}; b: T_{DG}: T_{GLEAM} - T_{SIF}, mm day^{-1}). T_{DM}, T_{DG}, LAI, and F_{wet} are sorted into 7 bins according to the 0-10th, 10-20th, …, 50-60th, and 60-70th percentiles of F_{wet}.

values within the intermediate LAI group still remain negative (Fig. 6b). Moreover, the mean T_{DG} for both low and intermediate LAI groups are relatively unresponsive to variations in F_{wet}, generally staying close to −1.5 mm day^{-1} (Fig. 6b). Such a pattern is also consistent with the underestimation of T_{GLEAM} compared to T_{SIF} noted in many regions worldwide (Fig. 5b).

5. Discussion

SIF, as one measure of plant photosynthetic activity observable by remote sensing, offers a new pathway to estimate stomatal conductance and transpiration rate across scales (Chen and Liu, 2020; Damm et al., 2018; Mohammed et al., 2019). However, the strategies that can be used to embed SIF in modelling GPP (and thus G_c and T) are different in their fidelity and applicability, and they generally belong to one of two categories: (1) empirical models that establish statistical relationships between SIF and GPP using in-situ measurements (e.g., EC flux towers), and extrapolate them to larger spatial scales (Guanter et al., 2014; Li and Xiao, 2022), and (2) mechanistic models that explicitly represent the processes associated with the SIF-GPP relationship (Gu et al., 2019; Liu et al., 2022). The performance of empirical SIF-GPP models may significantly decline in regions with a low density of flux towers. Also, it is difficult for empirical models to provide insights on mechanisms determining responses of T to changes in environmental conditions like VPD and SWC (Damm et al., 2021). By contrast, mechanistic models estimate GPP in a physically robust fashion without reliance on EC

measurements, making them more suitable for interpreting interactions between stomatal conductance, photosynthesis, transpiration, and environmental factors at scales larger than a single site. The incorporation of the rMLR model which is driven by satellite SIF observations and readily-available forcing data makes the proposed T estimation model not only physically defensible but also globally applicable.

Variations in the meteorological variables through the depth of the canopy lead to different transpiration rates within the canopy. For example, higher irradiance and higher VPD may result in more water loss through the stomata in the upper leaves compared with the leaves in the middle and lower canopy layers (Damm et al., 2009). As a result, upscaling approaches that simply assume that each leaf contributes equally to the canopy-level stomatal conductance or photosynthesis rate may introduce large biases. In contrast, total emitted fluorescence of all leaves (i.e., SIF_{tot}) represents the averaged SIF emission of all leaves in the canopy and, if translated into photosynthetic CO_2 assimilation mechanistically, should have a good potential to integrate varying contributions from all leaf layers to the canopy total fluxes of carbon uptake and/or water loss (Lu et al., 2020).

With the simultaneous use of SIF-derived T and estimates of VPD and SWC at the daily timescale, we show that VPD, rather than SWC, is the dominant driver of dryness stress on both G_c and T over most vegetated areas. However, it should be noted that the correlation between VPD and SWC tends to increase as the timescale increases from daily to monthly, and yearly (Liu et al., 2020), suggesting that SWC may play a more important role over longer time scales. With accumulating SIF data, the proposed T estimation model enables us to assess the relative contributions of VPD and SWC to G_c and T across different time scales in a physiologically meaningful way.

We acknowledge that this study has some limitations which require further research. The rMLR model currently has an advantage for large-scale applications over the original MLR model, but at the expense of incorporating PAR. Recognizing that PAR and SIF are highly correlated, our model appears somewhat redundant. For the purpose of simplifying the model framework and reducing uncertainties in estimating PAR, it is desirable to develop a q_L model driven by environmental variables available at regional/global scales. Under the assumption that PAR exerts a first-order control on q_L, recent studies (Chang et al., 2021; Feng et al., 2021; Han et al., 2022) have used parsimonious light response models for q_L. Nevertheless, more experiments are required to assess how q_L responds to other environmental factors including temperature, water, nutrient availability, and CO_2 concentration (Porcar-Castell, 2011; Takahashi et al., 2021; Yamori et al., 2011).

In this study, EC measurements were used to validate the SIF-based T estimates, which presents certain drawbacks, including the differing spatial scales between flux measurements and remote sensing data, as well as the limited number of EC flux sites available that meet the validation requirements. We acknowledge the potential of sap flow data as a valuable proxy for water vapor flux resulting from transpiration, offering a promising method for directly validating transpiration models. Yet, when utilizing sap flow data to evaluate global transpiration estimates, several limitations currently exist: (1) there is a mismatch between footprint of tree stem sap flow measurements representing small stand-level upscaling and relatively coarse grid cells used in estimating global transpiration (Kim et al., 2023; Li et al., 2023); (2) it is difficult to obtain information such as the number and type of plants in the simulation grid was not considered (Bittencourt et al., 2023); (3) the SAPFLUXNET database lacks data for the extremely tall trees and other growth forms such as shrubs, lianas, and other non-woody species (Liu et al., 2011; Lu et al., 2002; Poyatos et al., 2021). Considering these limitations, we believe that currently relying on EC data (assuming ET ≈ T) is more appropriate for assessing global T products.

The rMLR model still depends on empirical relationships and theoretical assumptions to estimate key variables like Φ_{PSII} and NPQ, which undoubtedly introduces uncertainties in estimating T. For instance, the parameters in these empirical formulas were calibrated over a limited range of plants (Bacour et al., 2019). These parameters might lead to uncertainties in estimating Φ_{PSII} and NPQ for other diverse ecosystems. Moreover, the methods we use to estimate Φ_{PSII} and NPQ may not adequately respond to stresses caused by factors other than light and heat, such as water deficit or the photoinhibition of reaction centers (Liu et al., 2022). Additionally, we were unable to capture the variation in Φ_{PSII} and NPQ across different layers of the canopy. Typically, sunlit leaves with higher light intensity and temperatures have lower Φ_{PSII} but higher NPQ compared to shaded leaves, which are subject to lower light and cooler temperatures (Gu et al., 2019).

Indeed, refining these estimations is an important future direction for improvement. However, these empirical relationships do not negate the potential of the mechanistic model. If we continue to rely solely on statistical methods to estimate A_{net}, our ability to do so will remain substantially limited by the number of observation sites, regardless of any advancements in methods for estimating Φ_{PSII} and NPQ. Conversely, the inherently mechanistic nature of the rMLR model ensures that any progress in estimating the key variables will simultaneously enhance the accuracy of A_{net}, and thereby T. In essence, mechanistic models, like the rMLR model in this study, provide a robust foundation for future research efforts in modelling T.

The values of a reported in the literature are highly variable between and within species. Ball (1988) reported that a varied in a wide range between 2.4 and 16.4 across a variety of C3 and C4 species. By fitting the BWB-Leuning equation to a dataset of eight forest types ranging from tropical to boreal trees, Medlyn et al. (2011) reported that a varied from 4.55 to 15.27. Particularly for C3 vegetation, a number of studies (Collatz et al., 1991; De Pury, 1995; Leuning, 1990) showed that a had a mean of 10.0, and a standard deviation of 2.0. Variation in growth temperature and CO_2 concentration may also cause large variations in the value of a (Bunce, 1998; Bunce, 2004; Miner et al., 2017). As there is little information on how a varies with species and growing conditions, we assumed here that a was a constant with a value of 10. However, more research is needed to better understand the response of a to variations in abiotic and biotic factors.

6. Conclusions

In this study, a SIF-based T estimation model was developed to mechanistically approximate A_{net} in the BWB-Leuning equation to constrain Gc as a key input for the PM modelling framework. The proposed model generally yielded good estimates of T for ecosystems with a dense canopy: the modeled T_{SIF} using satellite inputs and gridded meteorological data explained >70% of the T_{EC} variations for most forest types, 68% for croplands, and 72% for grasslands at the daily scale. Our results showed that T_{SIF} accounted for 32.36% of precipitation over vegetated land areas with valid data during the period 2019–2020. On a daily basis, VPD, rather than SWC, had the dominant role in determining dryness stress on both Gc and T_{SIF} over most vegetated areas. Compared with previous T modelling efforts, our model has one major advantage: it mechanistically converts satellite SIF observations into A_{net}, and so ingests more physiologically based information to constrain G_c and, eventually, T at a large scale. With these important improvements, the present model better unleashes the potential of SIF in modelling T, and thus advances our understanding of terrestrial carbon and water cycle feedbacks to climatic changes.

CRediT authorship contribution statement

Jingjing Yang: Conceptualization, Data curation, Methodology, Writing – original draft. **Zhunqiao Liu:** Methodology, Writing – review & editing. **Qiang Yu:** Resources. **Xiaoliang Lu:** Conceptualization, Funding acquisition, Methodology, Project administration, Supervision, Writing – review & editing.

Declaration of competing interest

The authors declare that they have no known competing financial interests or personal relationships that could have influenced the work reported in this paper.

Data availability

Data will be made available on request.

Acknowledgments

The authors would like to thank the three anonymous reviewers for their valuable comments and suggestions. The research was supported by the National Natural Science Foundation of China (Grant No. 41901293 to Z.L., 42071328 to X.L), the China Postdoctoral Science Foundation (Grant No. 2019 M663828 to Z.L.), and the Chinese Universities Scientific Fund (24520212452021125 to X.L.).

Appendix A. Definitions and methods for the nomenclature used in this study

Symbols	Definition	Unit	Method
T	Transpiration	g m^{-2} s^{-1}	Eq. (1)
R_n	Net radiation	W m^{-2}	Observed
G	Soil heat flux	W m^{-2}	Eq. (1)
ρ	Density of dry air	kg m^{-3}	1.2
C_p	Specific heat capacity of air	J kg^{-1} °C^{-1}	1013
VPD	Atmospheric vapor pressure deficit	kPa	Observed
g_a	Aerodynamic resistance for heat and water vapor	m s^{-1}	Eq. (S1a)
G_c	Canopy conductance to transpired water vapor	m s^{-1}	Eq. (2)
λ_v	Latent heat of vaporization	kJ kg^{-1}	2450
G_o	Residual conductance	mol m^{-2} s^{-1}	0.01
f_w	Soil water content dependent function	/	Eq. (20)
A_{net}	Net photosynthetic rate	μmol m^{-2} s^{-1}	Eq. (4)
C_s	Leaf surface CO_2 concentration	μmol mol^{-1}	Eq. (2)
G_{c_MODIS}	Canopy conductance obtained from the MOD16 algorithm (version 6.0)	m s^{-1}	Eq. (3a)
G_s^2	Leaf boundary-layer conductance	m s^{-1}	Eq. (3a)
G_s^1	Stomatal conductance per unit leaf area	m s^{-1}	Eq. (3a)
G_{CU}	Leaf cuticular conductance per unit leaf area	m s^{-1}	Eq. (3a)
LAI	Leaf area index		Observed
F_{wet}	Water cover fraction	%	Eq. (3b)
RH	Relative humidity	%	Observed
C_c	Chloroplastic CO_2 partial pressure	μbar or μmol mol^{-1}	Eq. (4)
C_i	Intercellular CO_2 concentration	μmol mol^{-1}	Eqs. (21)–(23)
Γ^*	Chloroplastic compensation point of CO_2	μbar	Eq. (13)
Φ_{PSII}	The quantum yield of photochemical quenching in PSII	/	Eq. (5)
NPQ	Nonphotochemical quenching	/	Eq. (15)
K_{DF}	The ratio between K_D and K_F	/	9
$SIF_{TOC\_FULL\_PSII}$	Broadband canopy SIF flux density emitted by PSII	μmol m^{-2} s^{-1}	Eq. (4)
$f_{esc\_P\text{-}C}$	The probability that a SIF photon escapes from the PSII light reactions to the top of the canopy	/	Eq. (19)
ξ	Fraction of total electron transport of mesophyll and bundle sheath allocated to mesophyll	/	0.4
R_d	Daytime leaf dark respiration	μmol m^{-2} s^{-1}	Eq. (12)
ETR	Electron transport rate in photosynthesis limited by the electron transport rate	μmol m^{-2} s^{-1}	Eq. (6)
ETR_{c_PSII}	Electron transport rate limited by the carboxylation rate	μmol m^{-2} s^{-1}	Eq. (8a)
PAR	Photochemically active radiation	μmol m^{-2} s^{-1}	Observed
f_{PAR}	Photosynthetically active radiation absorption efficiency	/	Observed
β	Partition of energy between the two photosystems	/	0.5
J_{max}	Maximum value of ETR under saturated light	μmol m^{-2} s^{-1}	Eq. (7a)
T_{air}	Air temperature	°C	Observed
J_{max_25}	J_{max} at a reference temperature of usually 25 °C	μmol m^{-2} s^{-1}	Eq. (7b)
V_{cmax25}	Maximum carboxylation capacity of Rubisco at 25 °C	μmol m^{-2} s^{-1}	Observed
A_C	Rubisco activity limited net photosynthesis rate	μmol m^{-2} s^{-1}	Eq. (8b)
V_{cmax}	Maximum carboxylation capacity of Rubisco	μmol m^{-2} s^{-1}	Eq. (11)
O	Oxygen partial pressure	mol mol^{-1}	Eq. (8b)
K_c	Michaelis-Menten constant of Rubisco for CO_2	mol mol^{-1}	Eq. (9)
K_{c25}	Michaelis-Menten constant of Rubisco for CO_2 at 25 °C	mol mol^{-1}	270
E_{Kc}	Activation energy	J mol^{-1}	80,990
R_{gas}	Universal gas constant	m^3 Pa mol^{-1} K^{-1}	8.3143
K_o	Michaelis-Menten constants of Rubisco for O_2	mol mol^{-1}	Eq. (10)
K_{o25}	Michaelis-Menten constants of Rubisco for O_2 at 25 °C	mol mol^{-1}	165,000
E_{Ko}	Activation energy	J mol^{-1}	23,720
E_{vcmax}	Activation energy	J mol^{-1}	65,330
E_{Rd}	Activation energy	J mol^{-1}	46,390
$S_{C/O}$	Relative CO_2/O_2 specificity factor for Rubisco	bar bar^{-1}	Eq. (14)
$E_{Sc/o}$	Activation energy	J mol^{-1}	−24,460
Φ_{PSII_max}	Maximum photosynthetic yield at the fully dark-adapted photosystems	/	0.8
f_{PSII}	ChlF contribution from PSII	%	Eq. (17)
Φ_{F_PSII}	The fluorescence yield in PSII at the steady-state condition	/	Eq. (18)
Φ_{F0_PSII}	The minimum fluorescence yield with a maximum proportion of open PSII reaction centers	/	0.02
K_D	The rate constant for constitutive heat loss	/	0.9
K_F	The rate constant for fluorescence emission	/	0.1
θ_S	Measured soil water content of top 100 cm soil layer	m^3 m^{-3}	Observed

(continued on next page)

(*continued*)

Symbols	Definition	Unit	Method
θ_F	Soil water content at the field capacity of the top 100 cm soil layer	/	Eq. (20)
θ_W	Soil water content at wilting point of the top 100 cm soil layer	/	Eq. (20)
C_a	Ambient air CO_2 partial pressure	μmol mol^{-1}	Eq. (21)
G_{c_co2}	Stomatal conductance for CO_2 at canopy scale	m s^{-1}	Eq. (22)
gl_{bl}	Leaf-scale boundary layer conductance	m s^{-1}	Eq. (S1a)
σ	Stefan-Boltzmann constant	W m^{-2} K^{-4}	5.6700e-08
R_{veg}	Vegetation far-red reflectance	/	Eq. (S3)
i_0	Canopy interceptance	/	Eq. (S5)
w	Leaf albedo	/	Eq. (19)
SZA	Solar zenith angle	°	Eq. (S4)
CI	clumping index	/	Eq. (S5)

Appendix B. Supplementary data

Supplementary data to this article can be found online at https://doi.org/10.1016/j.rse.2024.113998.

References

Anderegg, W.R.L., Konings, A.G., Trugman, A.T., Yu, K., Bowling, D.R., Gabbitas, R., Karp, D.S., Pacala, S., Sperry, J.S., Sulman, B.N., Zenes, N., 2018. Hydraulic diversity of forests regulates ecosystem resilience during drought. Nature. 561, 538–541.

Arain, M.A., Black, T.A., Barr, A.G., Jarvis, P.G., Massheder, J.M., Verseghy, D.L., Nesic, Z., 2002. Effects of seasonal and interannual climate variability on net ecosystem productivity of boreal deciduous and conifer forests. Can. J. For. Res. 32, 878–891.

Atkin, O.K., Bloomfield, K.J., Reich, P.B., Tjoelker, M.G., Asner, G.P., Bonal, D., Bonisch, G., Bradford, M.G., Cernusak, L.A., Cosio, E.G., Creek, D., Crous, K.Y., Domingues, T.F., Dukes, J.S., Egerton, J.J., Evans, J.R., Farquhar, G.D., Fyllas, N.M., Gauthier, P.P., Gloor, E., Gimeno, T.E., Griffin, K.L., Guerrieri, R., Heskel, M.A., Huntingford, C., Ishida, F.Y., Kattge, J., Lambers, H., Liddell, M.J., Lloyd, J., Lusk, C. H., Martin, R.E., Maksimov, A.P., Maximov, T.C., Malhi, Y., Medlyn, B.E., Meir, P., Mercado, L.M., Mirotchnick, N., Ng, D., Niinemets, U., O'Sullivan, O.S., Phillips, O. L., Poorter, L., Poot, P., Prentice, I.C., Salinas, N., Rowland, L.M., Ryan, M.G., Sitch, S., Slot, M., Smith, N.G., Turnbull, M.H., VanderWel, M.C., Valladares, F., Veneklaas, E.J., Weerasinghe, L.K., Wirth, C., Wright, I.J., Wythers, K.R., Xiang, J., Xiang, S., Zaragoza-Castells, J., 2015. Global variability in leaf respiration in relation to climate, plant functional types and leaf traits. New Phytol. 206, 614–636.

Bacour, C., Maignan, F., MacBean, N., Porcar-Castell, A., Flexas, J., Frankenberg, C., Peylin, P., Chevallier, F., Vuichard, N., Bastrikov, V., 2019. Improving estimates of gross primary productivity by assimilating solar-induced fluorescence satellite retrievals in a terrestrial biosphere model using a process-based SIF model. Eur. J. Vasc. Endovasc. Surg. 124, 3281–3306.

Ball, J.T., 1988. An Analysis of Stomatal Conductance. Stanford University.

Ball, J.T., Woodrow, I.E., Berry, J.A., 1987. A model predicting stomatal conductance and its contribution to the control of photosynthesis under different environmental conditions. Progress. Photosynth. Res. 221–224.

Beringer, J., Moore, C.E., Cleverly, J., Campbell, D.I., Cleugh, H., De Kauwe, M.G., Kirschbaum, M.U.F., Griebel, A., Grover, S., Huete, A., Hutley, L.B., Laubach, J., Van Niel, T., Arndt, S.K., Bennett, A.C., Cernusak, L.A., Eamus, D., Ewenz, C.M., Goodrich, J.P., Jiang, M., Hinko-Najera, N., Isaac, P., Hobeichi, S., Knauer, J., Koerber, G.R., Liddell, M., Ma, X., Macfarlane, C., McHugh, I.D., Medlyn, B.E., Meyer, W.S., Norton, A.J., Owens, J., Pitman, A., Pendall, E., Prober, S.M., Ray, R.L., Restrepo-Coupe, N., Rifai, S.W., Rowlings, D., Schipper, L., Silberstein, R.P., Teckentrup, L., Thompson, S.E., Ukkola, A.M., Wall, A., Wang, Y.P., Wardlaw, T.J., Woodgate, W., 2022. Bridge to the future: important lessons from 20 years of ecosystem observations made by the OzFlux network. Glob. Chang. Biol. 28, 3489–3514.

Bernacchi, C.J., Singsaas, E.L., Pimentel, C., Portis, A.R., Long, S.P., 2001. Improved temperature response functions for models of rubisco-limited photosynthesis. Plant Cell Environ. 24, 253–259.

Bernacchi, C.J., Portis, A.R., Nakano, H., von Caemmerer, S., Long, S.P., 2002. Temperature response of mesophyll conductance. Implications for the determination of rubisco enzyme kinetics and for limitations to photosynthesis in vivo. Plant Physiol. 130, 1992–1998.

Biederman, J.A., Scott, R.L., Goulden, M.L., Vargas, R., Litvak, M.E., Kolb, T.E., Yepez, E. A., Oechel, W.C., Blanken, P.D., Bell, T.W., Garatuza-Payan, J., Maurer, G.E., Dore, S., Burns, S.P., 2016. Terrestrial carbon balance in a drier world: the effects of water availability in southwestern North America. Glob. Chang. Biol. 22, 1867–1879.

Bittencourt, P., Rowland, L., Sitch, S., Poyatos, R., Miralles, D.G., Mencuccini, M., 2023. Bridging scales: An approach to evaluate the temporal patterns of global transpiration products using tree-scale sap flow data. Eur. J. Vasc. Endovasc. Surg. 128 e2022JG007308.

Bunce, J.A., 1998. Effects of environment during growth on the sensitivity of leaf conductance to changes in humidity. Glob. Chang. Biol. 4, 269–274.

Bunce, J.A., 2004. Carbon dioxide effects on stomatal responses to the environment and water use by crops under field conditions. Oecologia. 140, 1–10.

Chang, C.Y., Wen, J., Han, J., Kira, O., LeVonne, J., Melkonian, J., Riha, S.J., Skovira, J., Ng, S., Gu, L., Wood, J.D., Näthe, P., Sun, Y., 2021. Unpacking the drivers of diurnal dynamics of sun-induced chlorophyll fluorescence (SIF): canopy structure, plant physiology, instrument configuration and retrieval methods. Remote Sens. Environ. 265, 112672.

Chen, J.M., Leblanc, S.G., 2001. Multiple-scattering scheme useful for geometric optical modeling. IEEE Trans. Geosci. Remote Sens. 39, 1061–1071.

Chen, J.M., Liu, J., 2020. Evolution of evapotranspiration models using thermal and shortwave remote sensing data. Remote Sens. Environ. 237, 111594.

Chen, J.M., Wang, R., Liu, Y., He, L., Croft, H., Luo, X., Wang, H., Smith, N.G., Keenan, T. F., Prentice, I.C., Zhang, Y., Ju, W., Dong, N., 2022. Global datasets of leaf photosynthetic capacity for ecological and earth system research. Earth Syst. Sci. Data. 14, 4077–4093.

Chu, H., Luo, X., Ouyang, Z., Chan, W.S., Dengel, S., Biraud, S.C., Torn, M.S., Metzger, S., Kumar, J., Arain, M.A., 2021. Representativeness of Eddy-covariance flux footprints for areas surrounding AmeriFlux sites. Agric. For. Meteorol. 301, 108350.

Cleugh, H.A., Leuning, R., Mu, Q., Running, S.W., 2007. Regional evaporation estimates from flux tower and MODIS satellite data. Remote Sens. Environ. 106, 285–304.

Collatz, G., Ball, J., Grivet, C., Berry, J., 1991. Regulation of stomatal conductance and transpiration: a physiological model of canopy processes. Agric. For. Meteorol. 54, 107–136.

Croft, H., Chen, J.M., Wang, R., Mo, G., Luo, S., Luo, X., He, L., Gonsamo, A., Arabian, J., Zhang, Y., Simic-Milas, A., Noland, T.L., He, Y., Homolová, L., Malenovský, Z., Yi, Q., Beringer, J., Amiri, R., Hutley, L., Arellano, P., Stahl, C., Bonal, D., 2020. The global distribution of leaf chlorophyll content. Remote Sens. Environ. 236, 111479.

Damm, A., Elbers, J.A.N., Erler, A., Gioli, B., Hamdi, K., Hutjes, R., Kosvancova, M., Meroni, M., Miglietta, F., Moersch, A., Moreno, J., Schickling, A., Sonnenschein, R., Udelhoven, T., Van Der Linden, S., Hostert, P., Rascher, U.W.E., 2009. Remote sensing of sun-induced fluorescence to improve modeling of diurnal courses of gross primary production (GPP). Glob. Chang. Biol. 16, 171–186.

Damm, A., Paul-Limoges, E., Haghighi, E., Simmer, C., Morsdorf, F., Schneider, F.D., van der Tol, C., Migliavacca, M., Rascher, U., 2018. Remote sensing of plant-water relations: An overview and future perspectives. J. Plant Physiol. 227, 3–19.

Damm, A., Haghighi, E., Paul-Limoges, E., van der Tol, C., 2021. On the seasonal relation of sun-induced chlorophyll fluorescence and transpiration in a temperate mixed forest. Agric. For. Meteorol. 304–305.

Dawson, T.E., Goldsmith, G.R., 2018. The value of wet leaves. New Phytol. 219, 1156–1169.

De Pury, D.G.G., 1995. Scaling Photosynthesis and Water Use from Leaves to Paddocks. The Australian National University.

Desai, A.R., 2010. Climatic and phenological controls on coherent regional interannual variability of carbon dioxide flux in a heterogeneous landscape. J. Geophys. Res. 115, G00J02.

El-Madany, T.S., Carrara, A., Martín, M.P., Moreno, G., Kolle, O., Pacheco-Labrador, J., Weber, U., Wutzler, T., Reichstein, M., Migliavacca, M., 2020. Drought and heatwave impacts on semi-arid ecosystems' carbon fluxes along a precipitation gradient. Philos. Trans. R. Soc. B. 375, 20190519.

Farquhar, G.D., Von Caemmerer, S., Berry, J.A., 1980. A biochemical model of photosynthetic CO2 assimilation in leaves of C3 species. Planta. 149, 78–90.

Feng, H., Xu, T., Liu, L., Zhou, S., Zhao, J., Liu, S., Xu, Z., Mao, K., He, X., Zhu, Z., Chai, L., 2021. Modeling transpiration with sun-induced chlorophyll fluorescence observations via carbon-water coupling methods. Remote Sens. 13, 804.

Fernandez, I.J., Rustad, L.E., Lawrence, G.B., 1993. Estimating total soil mass, nutrient content, and trace metals in soils under a low elevation spruce-fir forest. Can. J. Soil Sci. 73, 317–328.

Fisher, J.B., Melton, F., Middleton, E., Hain, C., Anderson, M., Allen, R., McCabe, M.F., Hook, S., Baldocchi, D., Townsend, P.A., Kilic, A., Tu, K., Miralles, D.D., Perret, J., Lagouarde, J.-P., Waliser, D., Purdy, A.J., French, A., Schimel, D., Famiglietti, J.S., Stephens, G., Wood, E.F., 2017. The future of evapotranspiration: global

requirements for ecosystem functioning, carbon and climate feedbacks, agricultural management, and water resources. Water Resour. Res. 53, 2618–2626.
Flerchinger, G.N., Seyfried, M.S., 2014. Comparison of methods for estimating evapotranspiration in a small rangeland catchment. Vadose Zone J. 13.
Frankenberg, C., Fisher, J.B., Worden, J., Badgley, G., Saatchi, S.S., Lee, J.E., Toon, G.C., Butz, A., Jung, M., Kuze, A., Yokota, T., 2011. New global observations of the terrestrial carbon cycle from GOSAT: patterns of plant fluorescence with gross primary productivity. Geophys. Res. Lett. 38, 1–6.
Fu, Z., Ciais, P., Prentice, I.C., Gentine, P., Makowski, D., Bastos, A., Luo, X., Green, J.K., Stoy, P.C., Yang, H., Hajima, T., 2022. Atmospheric dryness reduces photosynthesis along a large range of soil water deficits. Nat. Commun. 13, 989.
Gelaro, R., McCarty, W., Suarez, M.J., Todling, R., Molod, A., Takacs, L., Randles, C., Darmenov, A., Bosilovich, M.G., Reichle, R., Wargan, K., Coy, L., Cullather, R., Draper, C., Akella, S., Buchard, V., Conaty, A., da Silva, A., Gu, W., Kim, G.K., Koster, R., Lucchesi, R., Merkova, D., Nielsen, J.E., Partyka, G., Pawson, S., Putman, W., Rienecker, M., Schubert, S.D., Sienkiewicz, M., Zhao, B., 2017. The modern-era retrospective analysis for research and applications, version 2 (MERRA-2). J. Clim. 30, 5419–5454.
Good, S.P., Noone, D., Bowen, G., 2015. Hydrologic connectivity constrains partitioning of global terrestrial water fluxes. Science. 349, 175–177.
Goodwell, A.E., Kumar, P., Fellows, A.W., Flerchinger, G.N., 2018. Dynamic process connectivity explains ecohydrologic responses to rainfall pulses and drought. P. Natl. Acad. Sci. 115, E8604–E8613.
Gu, L., Han, J., Wood, J.D., Chang, C.Y., Sun, Y., 2019. Sun-induced Chl fluorescence and its importance for biophysical modeling of photosynthesis based on light reactions. New Phytol. 223, 1179–1191.
Guanter, L., Frankenberg, C., Dudhia, A., Lewis, P.E., Gómez-Dans, J., Kuze, A., Suto, H., Grainger, R.G., 2012. Retrieval and global assessment of terrestrial chlorophyll fluorescence from GOSAT space measurements. Remote Sens. Environ. 121, 236–251.
Guanter, L., Zhang, Y., Jung, M., Joiner, J., Voigt, M., Berry, J.A., Frankenberg, C., Huete, A.R., Zarco-Tejada, P., Lee, J.E., Moran, M.S., Ponce-Campos, G., Beer, C., Camps-Valls, G., Buchmann, N., Gianelle, D., Klumpp, K., Cescatti, A., Baker, J.M., Griffis, T.J., 2014. Global and time-resolved monitoring of crop photosynthesis with chlorophyll fluorescence. Proc. Natl. Acad. Sci. U. S. A. 111, E1327–E1333.
Han, J., Chang, C.Y., Gu, L., Zhang, Y., Meeker, E.W., Magney, T.S., Walker, A.P., Wen, J., Kira, O., McNaull, S., Sun, Y., 2022. The physiological basis for estimating photosynthesis from Chla fluorescence. New Phytol. 234, 1206–1219.
He, L., Chen, J.M., Pisek, J., Schaaf, C.B., Strahler, A.H., 2012. Global clumping index map derived from the MODIS BRDF product. Remote Sens. Environ. 119, 118–130.
He, L., Magney, T., Dutta, D., Yin, Y., Köhler, P., Grossmann, K., Stutz, J., Dold, C., Hatfield, J., Guan, K., Peng, B., Frankenberg, C., 2020. From the ground to space: using solar-induced chlorophyll fluorescence to estimate crop productivity. Geophys. Res. Lett. 47 e2020GL087474.
Hwang, Y., Ryu, Y., Huang, Y., Kim, J., Iwata, H., Kang, M., 2020. Comprehensive assessments of carbon dynamics in an intermittently-irrigated rice paddy. Agric. For. Meteorol. 285-286, 107933.
Jaafar, H., Mourad, R., Schull, M., 2022. A global 30-m ET model (HSEB) using harmonized Landsat and Sentinel-2, MODIS and VIIRS: comparison to ECOSTRESS ET and LST. Remote Sens. Environ. 274, 112995.
Jasechko, S., Sharp, Z.D., Gibson, J.J., Birks, S.J., Yi, Y., Fawcett, P.J., 2013. Terrestrial water fluxes dominated by transpiration. Nature. 496, 347–350.
Joiner, J., Guanter, L., Lindstrot, R., Voigt, M., Vasilkov, A.P., Middleton, E.M., Huemmrich, K.F., Yoshida, Y., Frankenberg, C., 2013. Global monitoring of terrestrial chlorophyll fluorescence from moderate-spectral-resolution near-infrared satellite measurements: methodology, simulations, and application to GOME-2. Atmos. Meas. Tech. 6, 2803–2823.
Ju, W., Chen, J.M., Black, T.A., Barr, A.G., Liu, J., Chen, B., 2006. Modelling multi-year coupled carbon and water fluxes in a boreal aspen forest. Agric. For. Meteorol. 140, 136–151.
June, T., Evans, J.R., Farquhar, G.D., 2004. A simple new equation for the reversible temperature dependence of photosynthetic electron transport : a study on soybean leaf. Funct. Plant Biol. 31, 275–283.
Kim, J., Ryu, Y., Dechant, B., Lee, H., Kim, H.S., Kornfeld, A., Berry, J.A., 2021. Solar-induced chlorophyll fluorescence is non-linearly related to canopy photosynthesis in a temperate evergreen needleleaf forest during the fall transition. Remote Sens. Environ. 258, 112362.
Kim, Y., Park, H., Kimball, J.S., Colliander, A., McCabe, M.F., 2023. Global estimates of daily evapotranspiration using SMAP surface and root-zone soil moisture. Remote Sens. Environ. 298, 113803.
Köhler, P., Frankenberg, C., Magney, T.S., Guanter, L., Joiner, J., Landgraf, J., 2018. Global retrievals of solar induced chlorophyll fluorescence with TROPOMI: first results and inter-sensor comparison to OCO-2. Geophys. Res. Lett. 45, 456–463.
Kramer, D.M., Johnson, G., Kiirats, O., Edwards, G.E., 2004. New fluorescence parameters for the determination of QA redox state and excitation energy fluxes. Photosynth. Res. 79, 209–218.
Leuning, R., 1990. Modelling stomatal behaviour and and photosynthesis of Eucalyptus grandis. Funct. Plant Biol. 17, 159–175.
Leuning, R., Zhang, Y.Q., Rajaud, A., Cleugh, H., Tu, K., 2008. A simple surface conductance model to estimate regional evaporation using MODIS leaf area index and the Penman-Monteith equation. Water Resour. Res. 44.
Li, X., Xiao, J., 2022. TROPOMI observations allow for robust exploration of the relationship between solar-induced chlorophyll fluorescence and terrestrial gross primary production. Remote Sens. Environ. 268, 112748.
Li, S., Wang, G., Zhu, C., Hannemann, M., Poyatos, R., Lu, J., Li, J., Ullah, W., Hagan, D. F.T., García-García, A., Liu, Y., Liu, Q., Ma, S., Liu, Q., Sun, S., Zhao, F., Peng, J., 2023. Spatial patterns and recent temporal trends in global transpiration modelled using eco-evolutionary optimality. Agric. For. Meteorol. 342, 109702.
Liu, B., Zhao, W., Jin, B., 2011. The response of sap flow in desert shrubs to environmental variables in an arid region of China. Ecohydrology. 4, 448–457.
Liu, L., Gudmundsson, L., Hauser, M., Qin, D., Li, S., Seneviratne, S.I., 2020. Soil moisture dominates dryness stress on ecosystem production globally. Nat. Commun. 11, 4892.
Liu, Z., Zhao, F., Liu, X., Yu, Q., Wang, Y., Peng, X., Cai, H., Lu, X., 2022. Direct estimation of photosynthetic CO2 assimilation from solar-induced chlorophyll fluorescence (SIF). Remote Sens. Environ. 271, 112893.
Long, D., Singh, V.P., 2012. A two-source trapezoid model for evapotranspiration (TTME) from satellite imagery. Remote Sens. Environ. 121, 370–388.
Lu, P., Woo, K.C., Liu, Z.T., 2002. Estimation of whole-plant transpiration of bananas using sap flow measurements. J. Exp. Bot. 53, 1771–1779.
Lu, X., Liu, Z., An, S., Miralles, D.G., Maes, W., Liu, Y., Tang, J., 2018. Potential of solar-induced chlorophyll fluorescence to estimate transpiration in a temperate forest. Agric. For. Meteorol. 252, 75–87.
Lu, X., Liu, Z., Zhao, F., Tang, J., 2020. Comparison of total emitted solar-induced chlorophyll fluorescence (SIF) and top-of-canopy (TOC) SIF in estimating photosynthesis. Remote Sens. Environ. 251, 112083.
Luo, X., Croft, H., Chen, J.M., He, L., Keenan, T.F., 2019. Improved estimates of global terrestrial photosynthesis using information on leaf chlorophyll content. Glob. Chang. Biol. 25, 2499–2514.
Ma, Z., Xu, J., Ma, Y., Zhu, S., He, K., Zhang, S., Ma, W., Xu, X., 2022. AERA5-Asia: a long-term asian precipitation dataset (0.1°, 1-hourly, 1951–2015, Asia) anchoring the ERA5-land under the total volume control by APHRODITE. Bull. Am. Meteorol. Soc. 103, E1146–E1171.
Maes, W.H., Pagán, B.R., Martens, B., Gentine, P., Guanter, L., Steppe, K., Verhoest, N.E. C., Dorigo, W., Li, X., Xiao, J., Miralles, D.G., 2020. Sun-induced fluorescence closely linked to ecosystem transpiration as evidenced by satellite data and radiative transfer models. Remote Sens. Environ. 249, 112030.
Magney, T.S., Bowling, D.R., Logan, B.A., Grossmann, K., Stutz, J., Blanken, P.D., Burns, S.P., Cheng, R., Garcia, M.A., Khler, P., Lopez, S., Parazoo, N.C., Raczka, B., Schimel, D., Frankenberg, C., 2019. Mechanistic evidence for tracking the seasonality of photosynthesis with solar-induced fluorescence. Proc. Natl. Acad. Sci. U. S. A. 116, 11640–11645.
Martens, B., Miralles, D.G., Lievens, H., van der Schalie, R., de Jeu, R.A.M., Fernández-Prieto, D., Beck, H.E., Dorigo, W.A., Verhoest, N.E.C., 2017. GLEAM v3: satellite-based land evaporation and root-zone soil moisture. Geosci. Model Dev. 10, 1903–1925.
Medlyn, B.E., Duursma, R.A., Eamus, D., Ellsworth, D.S., Prentice, I.C., Barton, C.V.M., Crous, K.Y., De Angelis, P., Freeman, M., Wingate, L., 2011. Reconciling the optimal and empirical approaches to modelling stomatal conductance. Glob. Chang. Biol. 17, 2134–2144.
Metzger, S., Ayres, E., Durden, D., Florian, C., Lee, R., Lunch, C., Luo, H., Pingintha-Durden, N., Roberti, J.A., SanClements, M., Sturtevant, C., Xu, K., Zulueta, R.C., 2019. From NEON field sites to data portal: a community resource for surface–atmosphere research comes online. Bull. Am. Meteorol. Soc. 100, 2305–2325.
Miner, G.L., Bauerle, W.L., Baldocchi, D.D., 2017. Estimating the sensitivity of stomatal conductance to photosynthesis: a review. Plant Cell Environ. 40, 1214–1238.
Miralles, D.G., Gash, J.H., Holmes, T.R.H., de Jeu, R.A.M., Dolman, A.J., 2010. Global canopy interception from satellite observations. J. Geophys. Res. 115.
Miralles, D.G., Jiménez, C., Jung, M., Michel, D., Ershadi, A., McCabe, M.F., Hirschi, M., Martens, B., Dolman, A.J., Fisher, J.B., Mu, Q., Seneviratne, S.I., Wood, E.F., Fernández-Prieto, D., 2016. The WACMOS-ET project – part 2: evaluation of global terrestrial evaporation data sets. Hydrol. Earth Syst. Sci. 20, 823–842.
Mohammed, G.H., Colombo, R., Middleton, E.M., Rascher, U., van der Tol, C., Nedbal, L., Goulas, Y., Perez-Priego, O., Damm, A., Meroni, M., Joiner, J., Cogliati, S., Verhoef, W., Malenovsky, Z., Gastellu-Etchegorry, J.P., Miller, J.R., Guanter, L., Moreno, J., Moya, I., Berry, J.A., Frankenberg, C., Zarco-Tejada, P.J., 2019. Remote sensing of solar-induced chlorophyll fluorescence (SIF) in vegetation: 50 years of progress. Remote Sens. Environ. 231, 111177.
Monteith, J.L., 1965. Evaporation and environment. Symp. Soc. Exp. Biol. 19, 205–234.
Montzka, C., Herbst, M., Weihermüller, L., Verhoef, A., Vereecken, H., 2017. A global data set of soil hydraulic properties and sub-grid variability of soil water retention and hydraulic conductivity curves. Earth Syst. Sci. Data. 9, 529–543.
Mu, Q., Heinsch, F.A., Zhao, M., Running, S.W., 2007. Development of a global evapotranspiration algorithm based on MODIS and global meteorology data. Remote Sens. Environ. 111, 519–536.
Mu, Q., Zhao, M., Running, S.W., 2011. Improvements to a MODIS global terrestrial evapotranspiration algorithm. Remote Sens. Environ. 115, 1781–1800.
Myneni, R., Knyazikhin, Y., Park, T., 2015. In: NASA (Ed.), MCD15A3H MODIS/Terra+ Aqua Leaf Area Index/FPAR 4-Day L4 Global 500m SIN Grid V006.
Norman, J.M., Kustas, W.P., Humes, K.S., 1995. Source approach for estimating soil and vegetation energy fluxes in observations of directional radiometric surface temperature. Agric. For. Meteorol. 77, 263–293.
Porcar-Castell, A., 2011. A high-resolution portrait of the annual dynamics of photochemical and non-photochemical quenching in needles of Pinus sylvestris. Physiol. Plant. 143, 139–153.
Poyatos, R., Granda, V., Flo, V., Adams, M.A., Adorján, B., Aguadé, D., Aidar, M.P.M., Allen, S., Alvarado-Barrientos, M.S., Anderson-Teixeira, K.J., Aparecido, L.M., Arain, M.A., Aranda, I., Asbjornsen, H., Baxter, R., Beamesderfer, E., Berry, Z.C., Berveiller, D., Blakely, B., Boggs, J., Bohrer, G., Bolstad, P.V., Bonal, D., Bracho, R., Brito, P., Brodeur, J., Casanoves, F., Chave, J., Chen, H., Cisneros, C., Clark, K., Cremonese, E., Dang, H., David, J.S., David, T.S., Delpierre, N., Desai, A.R., Do, F.C.,

Dohnal, M., Domec, J.-C., Dzikiti, S., Edgar, C., Eichstaedt, R., El-Madany, T.S., Elbers, J., Eller, C.B., Euskirchen, E.S., Ewers, B., Fonti, P., Forner, A., Forrester, D.I., Freitas, H.C., Galvagno, M., Garcia-Tejera, O., Ghimire, C.P., Gimeno, T.E., Grace, J., Granier, A., Griebel, A., Guangyu, Y., Gush, M.B., Hanson, P.J., Hasselquist, N.J., Heinrich, I., Hernandez-Santana, V., Herrmann, V., Hölttä, T., Holwerda, F., Irvine, J., Isarangkool Na Ayutthaya, S., Jarvis, P.G., Jochheim, H., Joly, C.A., Kaplick, J., Kim, H.S., Klemedtsson, L., Kropp, H., Lagergren, F., Lane, P., Lang, P., Lapenas, A., Lechuga, V., Lee, M., Leuschner, C., Limousin, J.-M., Linares, J.C., Linderson, M.-L., Lindroth, A., Llorens, P., López-Bernal, Á., Loranty, M.M., Lüttschwager, D., Macinnis-Ng, C., Maréchaux, I., Martin, T.A., Matheny, A., McDowell, N., McMahon, S., Meir, P., Mészáros, I., Migliavacca, M., Mitchell, P., Mölder, M., Montagnani, L., Moore, G.W., Nakada, R., Niu, F., Nolan, R.H., Norby, R., Novick, K., Oberhuber, W., Obojes, N., Oishi, A.C., Oliveira, R.S., Oren, R., Ourcival, J.-M., Paljakka, T., Perez-Priego, O., Peri, P.L., Peters, R.L., Pfautsch, S., Pockman, W.T., Preisler, Y., Rascher, K., Robinson, G., Rocha, H., Rocheteau, A., Röll, A., Rosado, B.H.P., Rowland, L., Rubtsov, A.V., Sabaté, S., Salmon, Y., Salomón, R.L., Sánchez-Costa, E., Schäfer, K.V.R., Schuldt, B., Shashkin, A., Stahl, C., Stojanović, M., Suárez, J.C., Sun, G., Szatniewska, J., Tatarinov, F., Tesař, M., Thomas, F.M., Tor-ngern, P., Urban, J., Valladares, F., van der Tol, C., van Meerveld, I., Varlagin, A., Voigt, H., Warren, J., Werner, C., Werner, W., Wieser, G., Wingate, L., Wullschleger, S., Yi, K., Zweifel, R., Steppe, K., Mencuccini, M., Martínez-Vilalta, J., 2021. Global transpiration data from sap flow measurements: the SAPFLUXNET database. Earth Syst. Sci. Data. 13, 2607–2649.

Priestley, C.H.B., Taylor, R.J., 1972. On the assessment of surface heat flux and evaporation using large-scale parameters. Mon. Weather Rev. 100, 81–92.

Prober, S.M., Thiele, K.R., Rundel, P.W., Yates, C.J., Berry, S.L., Byrne, M., Christidis, L., Gosper, C.R., Grierson, P.F., Lemson, K., Lyons, T., Macfarlane, C., O'Connor, M.H., Scott, J.K., Standish, R.J., Stock, W.D., van Etten, E.J.B., Wardell-Johnson, G.W., Watson, A., 2011. Facilitating adaptation of biodiversity to climate change: a conceptual framework applied to the world's largest Mediterranean-climate woodland. Clim. Chang. 110, 227–248.

Reich, P.B., Walters, M.B., Ellsworth, D.S., Vose, J.M., Volin, J.C., Gresham, C., Bowman, W.D., 1998. Relationships of leaf dark respiration to leaf nitrogen, specific leaf area and leaf life-span: a test across biomes and functional groups. Oecologia. 114, 471–482.

Restrepo-Coupe, N., da Rocha, H.R., Hutyra, L.R., da Araujo, A.C., Borma, L.S., Christoffersen, B., Cabral, O.M.R., de Camargo, P.B., Cardoso, F.L., da Costa, A.C.L., Fitzjarrald, D.R., Goulden, M.L., Kruijt, B., Maia, J.M.F., Malhi, Y.S., Manzi, A.O., Miller, S.D., Nobre, A.D., von Randow, C., Sá, L.D.A., Sakai, R.K., Tota, J., Wofsy, S. C., Zanchi, F.B., Saleska, S.R., 2013. What drives the seasonality of photosynthesis across the Amazon basin? A cross-site analysis of eddy flux tower measurements from the Brasil flux network. Agric. For. Meteorol. 182-183, 128–144.

Running, S.W., Kimball, J.S., 2005. Satellite-Based Analysis of Ecological Controls for Land-Surface Evaporation Resistance. Encyclopedia of Hydrological Sciences. Wiley, Hoboken, NJ.

Ryu, Y., Baldocchi, D.D., Kobayashi, H., van Ingen, C., Li, J., Black, T.A., Beringer, J., van Gorsel, E., Knohl, A., Law, B.E., Roupsard, O., 2011. Integration of MODIS Land and Atmosphere Products with a Coupled-Process Model to Estimate Gross Primary Productivity and Evapotranspiration from 1 Km to Global Scales. Global Biogeochem, Cycles, p. 25.

Sancho-Knapik, D., Mendoza-Herrer, Ó., Alonso-Forn, D., Saz, M.Á., Martín-Sánchez, R., dos Santos Silva, J.V., Ogee, J., Peguero-Pina, J.J., Gil-Pelegrín, E., Ferrio, J.P., 2022. Vapor pressure deficit constrains transpiration and photosynthesis in holm oak: a comparison of three methods during summer drought. Agric. For. Meteorol. 327, 109218.

Sardans, J., Grau, O., Chen, H.Y.H., Janssens, I.A., Ciais, P., Piao, S., Penuelas, J., 2017. Changes in nutrient concentrations of leaves and roots in response to global change factors. Glob. Chang. Biol. 23, 3849–3856.

Shan, N., Ju, W., Migliavacca, M., Martini, D., Guanter, L., Chen, J., Goulas, Y., Zhang, Y., 2019. Modeling canopy conductance and transpiration from solar-induced chlorophyll fluorescence. Agric. For. Meteorol. 268, 189–201.

Shan, N., Zhang, Y., Chen, J.M., Ju, W., Migliavacca, M., Peñuelas, J., Yang, X., Zhang, Z., Nelson, J.A., Goulas, Y., 2021. A model for estimating transpiration from remotely sensed solar-induced chlorophyll fluorescence. Remote Sens. Environ. 252, 112134.

Sulla-Menashe, D., Friedl, M.A., 2018. User Guide to Collection 6 MODIS Land Cover (MCD12Q1 and MCD12C1) Product. USGS, Reston, VA, USA, pp. 1–18.

Sulman, B.N., Roman, D.T., Yi, K., Wang, L., Phillips, R.P., Novick, K.A., 2016. High atmospheric demand for water can limit forest carbon uptake and transpiration as severely as dry soil. Geophys. Res. Lett. 43, 9686–9695.

Takahashi, Y., Wada, S., Noguchi, K., Miyake, C., Makino, A., Suzuki, Y., 2021. Photochemistry of photosystems II and I in rice plants grown under different N levels at normal and high temperature. Plant Cell Physiol. 62, 1121–1130.

Thornton, P.E., 1998. Regional Ecosystem Simulation: Combining Surface-and Satellite-Based Observations to Study Linkages between Terrestrial Energy and Mass Budgets. University of Montana, Thesis, p. 1015.

Trenberth, K.E., Fasullo, J., Kiehl, J., 2009. Earth's global energy budget. Bull. Am. Meteorol. Soc. 90, 311–323.

van der Tol, C., Verhoef, W., Timmermans, J., Verhoef, A., Su, Z., 2009. An integrated model of soil-canopy spectral radiances, photosynthesis, fluorescence, temperature and energy balance. Biogeosciences. 6, 3109–3129.

van der Tol, C., Berry, J.A., Campbell, P.K., Rascher, U., 2014. Models of fluorescence and photosynthesis for interpreting measurements of solar-induced chlorophyll fluorescence. Eur. J. Vasc. Endovasc. Surg. 119, 2312–2327.

Von Caemmerer, S., 2000. Biochemical Models of Leaf Photosynthesis: Csiro Publishing.

Wang, Y.P., Leuning, R., 1998. A two-leaf model for canopy conductance, photosynthesis and partitioning of available energy I: model description and comparison with a multi-layered model. Agric. For. Meteorol. 91, 89–111.

Wang, Q., He, Q., Zhou, G., 2018. Applicability of common stomatal conductance models in maize under varying soil moisture conditions. Sci. Total Environ. 628-629, 141–149.

Wang, X., Biederman, J.A., Knowles, J.F., Scott, R.L., Turner, A.J., Dannenberg, M.P., Köhler, P., Frankenberg, C., Litvak, M.E., Flerchinger, G.N., Law, B.E., Kwon, H., Reed, S.C., Parton, W.J., Barron-Gafford, G.A., Smith, W.K., 2022a. Satellite solar-induced chlorophyll fluorescence and near-infrared reflectance capture complementary aspects of dryland vegetation productivity dynamics. Remote Sens. Environ. 270, 112858.

Wang, Y., Kohler, P., Braghiere, R.K., Longo, M., Doughty, R., Bloom, A.A., Frankenberg, C., 2022b. GriddingMachine, a database and software for earth system modeling at global and regional scales. Sci. Data. 9, 258.

Wood, D.A., 2022. Net ecosystem exchange comparative analysis of the relative influence of recorded variables in well monitored ecosystems. Ecol. Complex. 50, 100998.

Wu, A., Doherty, A., Farquhar, G., Hammer, G.L., 2017. Simulating daily field crop canopy photosynthesis: an integrated software package. Funct. Plant Biol. 45, 362–377.

Wu, A., Hammer, G.L., Doherty, A., von Caemmerer, S., Farquhar, G.D., 2019. Quantifying impacts of enhancing photosynthesis on crop yield. Nat. Plants. 5, 380–388.

Wu, J., Feng, Y., Liang, L., He, X., Zeng, Z., 2022. Assessing evapotranspiration observed from ECOSTRESS using flux measurements in agroecosystems. Agric. Water Manag. 269, 107706.

Xiao, J., Davis, K.J., Urban, N.M., Keller, K., Saliendra, N.Z., 2011. Upscaling carbon fluxes from towers to the regional scale: influence of parameter variability and land cover representation on regional flux estimates. J. Geophys. Res. 116.

Xiao, J., Davis, K.J., Urban, N.M., Keller, K., 2014. Uncertainty in model parameters and regional carbon fluxes: a model-data fusion approach. Agric. For. Meteorol. 189-190, 175–186.

Yamori, W., Sakata, N., Suzuki, Y., Shikanai, T., Makino, A., 2011. Cyclic electron flow around photosystem I via chloroplast NAD(P)H dehydrogenase (NDH) complex performs a significant physiological role during photosynthesis and plant growth at low temperature in rice. Plant J. 68, 966–976.

Yang, Y., Shang, S., 2013. A hybrid dual-source scheme and trapezoid framework-based evapotranspiration model (HTEM) using satellite images: algorithm and model test. J. Geophys. Res. Atmos. 118, 2284–2300.

Yang, P., van der Tol, C., 2018. Linking canopy scattering of far-red sun-induced chlorophyll fluorescence with reflectance. Remote Sens. Environ. 209, 456–467.

Yang, X., Tang, J., Mustard, J.F., Lee, J.-E., Rossini, M., Joiner, J., Munger, J.W., Kornfeld, A., Richardson, A.D., 2015. Solar-induced chlorophyll fluorescence that correlates with canopy photosynthesis on diurnal and seasonal scales in a temperate deciduous forest. Geophys. Res. Lett. 42, 2977–2987.

Yang, H., Yang, X., Zhang, Y., Heskel, M.A., Lu, X., Munger, J.W., Sun, S., Tang, J., 2017. Chlorophyll fluorescence tracks seasonal variations of photosynthesis from leaf to canopy in a temperate forest. Glob. Chang. Biol. 23, 2874–2886.

Yin, X., Struik, P.C., 2009. C3 and C4 photosynthesis models: An overview from the perspective of crop modelling. NJAS: Wageningen. J. Life Sci. 57, 27–38.

Zhang, Y., Chiew, F.H.S., Peña-Arancibia, J., Sun, F., Li, H., Leuning, R., 2017. Global variation of transpiration and soil evaporation and the role of their major climate drivers. J. Geophys. Res. Atmos. 122, 6868–6881.

Zhang, Z., Chen, J.M., Guanter, L., He, L., Zhang, Y., 2019. From canopy-leaving to total canopy far-red fluorescence emission for remote sensing of photosynthesis: first results from TROPOMI. Geophys. Res. Lett. 46, 12030–12040.

Zhang, Z., Zhang, Y., Zhang, Y., Gobron, N., Frankenberg, C., Wang, S., Li, Z., 2020. The potential of satellite FPAR product for GPP estimation: An indirect evaluation using solar-induced chlorophyll fluorescence. Remote Sens. Environ. 240, 111686.

Zheng, C., Jia, L., 2020. Global canopy rainfall interception loss derived from satellite earth observations. Ecohydrology. 13.